NAQPMS-PDAF v2.0: A Novel Hybrid Nonlinear Data Assimilation System for Improved Simulation of PM$_{2.5}$ Chemical Components

Hongyi Li[1, 3], Ting Yang[1], Lars Nerger[4], Dawei Zhang[2], Di Zhang[2], Guigang Tang[2], Haibo Wang[1], Yele Sun[1, 3], Pingqing Fu[5], Hang Su[1, 6], Zifa Wang[1, 3]

[1]State Key Laboratory of Atmospheric Boundary Layer Physics and Atmospheric Chemistry (LAPC), Institute of Atmospheric Physics, Chinese Academy of Sciences, Beijing 100029, China.

[2]China National Environmental Monitoring Centre, Beijing, China

[3]College of Earth and Planetary Sciences, University of Chinese Academy of Sciences, Beijing 100049, China

[4]Alfred Wegener Institute, Helmholtz Center for Polar und Marine Research, Bremerhaven, Germany

[5]Institute of Surface-Earth System Science, School of Earth System Science, Tianjin University, Tianjin 300072, China

[6]Max Planck Institute for Chemistry, Mainz, Germany

Correspondence to: Ting Yang (tingyang@mail.iap.ac.cn)

Abstract. Identifying PM$_{2.5}$ chemical components is crucial for formulating emission strategies, estimating radiative forcing, and assessing human health effects. However, accurately describing spatiotemporal variations of PM$_{2.5}$ chemical components remains a challenge. In our earlier work, we developed an aerosol extinction coefficient data assimilation (DA) system (NAQPMS-PDAF v1.0) suboptimal for chemical components. This paper introduces a novel hybrid nonlinear chemical DA system (NAQPMS-PDAF v2.0) to accurately interpret key chemical components (SO$_4^{2-}$, NO$_3^-$, NH$_4^+$, OC, and EC). NAQPMS-PDAF v2.0 improves upon v1.0 by effectively handling and balancing stability and nonlinearity in chemical DA, which is achieved by incorporating the non-Gaussian-distribution ensemble perturbation and hybrid Localized Kalman-Nonlinear Ensemble Transform Filter with an adaptive forgetting factor for the first time. The dependence tests demonstrate that NAQPMS-PDAF v2.0 provides excellent DA results with a minimal ensemble size of 10, surpassing previous reports and v1.0. A one-month DA experiment shows that the analysis field generated by NAQPMS-PDAF v2.0 is in good agreement with observations, especially in reducing the underestimation of NH$_4^+$ and NO$_3^-$ and the overestimation of SO$_4^{2-}$, OC, and EC. In particular, the CORR values for NO$_3^-$, OC, and EC are above 0.96, and R^2 values are above 0.93. NAQPMS-PDAF v2.0 also demonstrates superior spatiotemporal interpretation, with most DA sites showing improvements of over 50%-200% in CORR and over 50%-90% in RMSE for the five chemical components. Compared to the poor performance in global reanalysis dataset (CORR: 0.42-0.55, RMSE: 4.51-12.27 μg/m^3) and NAQPMS-PDAF v1.0 (CORR: 0.35-0.98, RMSE: 2.46-15.50 μg/m^3), NAQPMS-PDAF v2.0 has the highest CORR of 0.86-0.99 and the lowest RMSE of 0.14-3.18 μg/m^3. The uncertainties in ensemble DA are also examined, further highlighting the potential of NAQPMS-PDAF v2.0 for advancing aerosol chemical component studies.

1 Introduction

PM$_{2.5}$ is a complex mixture of various chemical fractions, mainly including sulfate (SO$_4^{2-}$), nitrate (NO$_3^-$), ammonium (NH$_4^+$), organic carbon (OC), and elemental carbon (EC). These chemical components exert diverse influences on the atmospheric environment (Khanna et al., 2018), human health (Bell et al., 2007; Schlesinger, 2007; Li et al., 2022a; Alves et al., 2023), and climate change (Schult et al., 1997; Park et al., 2014; Wilcox et al., 2016). However, current detection technologies, such as direct observation by sampling and chemical analysis (Zhang et al., 2015; Ming et al., 2017), ground-based remote-sensing inversion (Nishizawa et al., 2008; Nishizawa et al., 2011; Nishizawa et al., 2017), and observation-based machine learning (Lin et al., 2022; Su Lee et al., 2023; Li et al., 2025), are insufficient in interpreting spatiotemporally continuous information of PM$_{2.5}$ chemical components due to the limited number of observation sites or platforms. Although atmospheric chemistry transport models (CTMs) (Wang et al., 2014; Wang et al., 2015; Jia et al., 2017; Yang et al., 2019; Li et al., 2020; Lv et al., 2020) are widely used to characterize the spatiotemporal distribution of multiple chemical species, CTMs are constrained by uncertainties in initial-boundary conditions, physiochemical mechanisms, emission inventories, and meteorological fields (Sax and Isakov, 2003; Mallet and Sportisse, 2006; Rodriguez et al., 2007; Chang et al., 2015; Miao et al., 2020; Xie et al., 2022), resulting in notable discrepancies between the model simulations and accurate observations.

Data assimilation (DA) offers a solution to integrate the multi-source observations, CTMs, and their uncertainties effectively to enhance the simulation and forecasting capabilities of CTMs. Variational methods (3D-Var/4D-Var) (Talagrand and Courtier, 1987), Ensemble Kalman Filter (EnKF) (Evensen, 1994; Evensen, 2003), EnKF-variants (EnKFs) (Bishop et al., 2001; Tippett et al., 2003; Hunt et al., 2007; Nerger et al., 2012), and hybrid EnKF-Var methods (Hamill and Snyder, 2000; Schwartz et al., 2014) are most widely applied in DA. However, variational methods have a flow-independent Background Error Covariance (BEC) with the assumption of isotropic, static, and uniform characteristics, and they need to develop the tangent linear adjoint model, which is difficult to practice for complex models. Although EnKFs and hybrid EnKF-Var methods have a flow-dependent BEC, they are sensitive to inadequate ensemble sampling and have high computational costs. Importantly, these methods cannot address model nonlinearity and non-Gaussian error distribution, yielding suboptimal results for DA in highly nonlinear CTMs.

Currently, nonlinear filters, such as Particle Filter (PF) (Gordon et al., 1993) and Nonlinear Ensemble Transform Filter (NETF) (Tödter and Ahrens, 2015), have been proposed to approximate the complete posterior probability distribution of model states and provide a better representation of non-Gaussian information based on Monte Carlo random sampling and Bayesian theory. However, PF is unstable and susceptible to filter degeneration compared to EnKFs. In a recent study, Nerger (2022) proposed the hybrid Kalman-Nonlinear Ensemble Transform Filter (KNETF) to achieve excellent DA performance in the Lorenz-63 and

62 Lorenz-96 model with a smaller ensemble size, which combines the stability of EnKFs and the nonlinearity of NETF (Nerger,

63 2022). However, to the author's knowledge, this algorithm has not been applied to the chemical DA of CTMs.

64

65 Studies on chemical DA involve the assimilation of aerosol optical properties, such as aerosol optical depth (AOD) and

66 extinction coefficient (EXT), and the particulate matters (PMs), such as the mass concentrations of $PM_{2.5}$ and PM_{10}. The

67 commonly AOD observations for DA include OMI-AOD (Ali et al., 2013), MODIS-AOD (Zhang et al., 2008; Huneeus et al.,

68 2012; Huneeus et al., 2013; Rubin and Collins, 2014; Lynch et al., 2016; Werner et al., 2019; Kumar et al., 2020), AERONET-

69 AOD (Schutgens et al., 2010; Li et al., 2016), Sun-Sky Photometer-Multiband AOD (Chang et al., 2021), GOCI-AOD (Saide

70 et al., 2014; Luo et al., 2020; Kim et al., 2021), and Fengyun/Himawari8-AOD (Bao et al., 2019; Jin et al., 2019; Xia et al.,

71 2019; Xia et al., 2020). These studies indicated that AOD observations can enhance the accuracy of aerosol simulation and

72 forecast. Compared to AOD, EXT DA effectively improves the interpretation of aerosol vertical distribution (Zhang et al.,

73 2014; Cheng et al., 2019; Wang et al., 2022). Additionally, the simultaneous DA of aerosol optical properties and PMs is widely

74 applied in aerosol studies (Tang et al., 2015; Chai et al., 2017). According to our literature review (Yang et al., 2023), there is

75 currently no DA study on aerosol chemical components due to the limited DA influence of PMs and AOD on chemical

76 compositions (Chang et al., 2021) and the limited chemical observations with an extensive spatial range. Moreover, the aerosol

77 chemical components exhibit nonlinearity and a non-Gaussian distribution (Ha, 2022), while current main-stream algorithms,

78 such as variational methods or EnKFs, are suboptimal for chemical component DA.

79

80 In our previous work, we developed an aerosol vertical DA system (NAQPMS-PDAF v1.0) based on EnKFs to improve the

81 simulation of the extinction coefficient vertical profile (Wang et al., 2022). In this study, we present a novel hybrid nonlinear

82 DA system (NAQPMS-PDAF v2.0) towards various $PM_{2.5}$ chemical components through online integration of Parallel Data

83 Assimilation Framework (PDAF, version 2.1, released on February 21st, 2023), Observation Module Infrastructure (OMI) and

84 Nested Air Quality Prediction Model System (NAQPMS). We collected 1-month hourly surface observations of five $PM_{2.5}$

85 chemical components (NH_4^+, SO_4^{2-}, NO_3^-, OC, and EC) over Northern China and surrounding areas. We utilized the hybrid

86 Localized Kalman-Nonlinear Ensemble Transform Filter (LKNETF) to generate a high-resolution and high-accuracy

87 reanalysis dataset of $PM_{2.5}$ chemical components for the first time. Notably, the ensemble members in NAQPMS-PDAF v2.0

88 are generated by perturbing emission species based on their uncertainties and non-Gaussian distribution assumption. Section

89 2 briefly introduces NAQPMS and PDAF v2.1 with OMI, respectively, and details the development of NAQPMS-PDAF v2.0,

90 including system structure, configuration, ensemble generation, and LKNETF algorithm. The data used in this study and

91 experimental settings are also described in Section 2. Section 3 presents the DA results, including an evaluation of

92 dependencies, performance, and external comparisons, as well as a discussion of the ensemble DA uncertainty. Section 4

93 summarizes the conclusions and outlook.

2 Method and data

2.1 NAQPMS

The Nested Air Quality Prediction Modeling System (NAQPMS), developed by the Institute of Atmospheric Physics (IAP), Chinese Academy of Sciences (CAS), is used to provide background fields for key aerosol chemical components in this study. NAQPMS is a multi-scale gridded 3-dimensional Eulerian chemical transport model based on continuity equations. The nested grids in the horizontal direction enable data exchange between different domains. Applying terrain-following coordinates in the vertical direction mitigates numerical calculation errors to enhance model accuracy. The NAQPMS comprises an input section, a numerical computation section, and an output section. The input section incorporates static terrain data, emission inventories, meteorological fields, and initial-boundary conditions. The numerical computation section performs multiple physicochemical process calculations, including the advection process, eddy diffusion, dry deposition, wet scavenging, gas-phase chemistry, aqueous chemistry, aerosol physicochemical processes (including heterogeneous reactions at the aerosol surface), and other processes. The schemes and features of the physicochemical processes are summarized in Table S1. The output section is responsible for model post-processing, data diagnostics, and source identification.

NAQPMS is capable of characterizing the three-dimensional spatiotemporal distribution of various atmospheric compositions at global and regional scales and has been widely used in atmospheric pollution and chemistry research, such as O_3 pollution (Wang et al., 2001), haze episodes (Wang et al., 2014; Du et al., 2021), regional transport (Wang et al., 2017; Wang et al., 2019), source identification (Li et al., 2022b), air quality simulation at global scale (Ye et al., 2021) and at urban-street scale (Wang et al., 2023), and acid deposition (Ge et al., 2014).

2.2 PDAF v2.1 with OMI

The Parallel Data Assimilation Framework (PDAF, https://pdaf.awi.de/trac/wiki) is an open-source and high-expandability software developed by the Alfred Wegener Institute (AWI) in Germany to integrate observations, numerical models, and assimilation systems for DA tasks, widely applied in meteorology, oceanography, land surface and atmospheric chemistry (Kurtz et al., 2016; Nerger et al., 2020; Mingari et al., 2022; Strebel et al., 2022; Wang et al., 2022; Yu et al., 2022). The initial version of PDAF (PDAF v1.0) was released in 2004. It has undergone continuous improvements and updates, with major updates including the introduction of Ensemble Transform Kalman Filter (ETKF) and its localized variant (LETKF) in version 1.6, the implementation of PDAF-OMI (Observation Module Infrastructure) in version 1.16, the integration of 3D-Var methods in version 2.0, and the incorporation of the hybrid KNETF and its localized variant (LKNETF) for the first time in version 2.1, which was released in 2023 to handle the complex DA situations, such as the nonlinearity of system and non-Gaussian error distribution of model state. Notably, the version of PDAF coupled in NAQPMS-PDAF v1.0 is PDAF v1.15 (released in 2019),

124 implying that NAQPMS-PDAF v1.0 has more limited applicability and functionality. In this work, the PDAF v2.1 is coupled

125 in NAQPMS-PDAF v2.0.

126

127 PDAF has offline and online modes. For the offline mode, PDAF and the model perform separately without coupling, obviating

128 the need to modify the model code. For the online mode, PDAF is coupled with the model, and model calculation and data

129 assimilation are performed continuously. Compared to the offline mode, the online coupling has several advantages. Firstly,

130 the initialization of the PDAF and the model is integrated, necessitating a single execution rather than two separate executions.

131 Secondly, the model integration result can be directly passed to PDAF for data assimilation. Additionally, the assimilation

132 result of PDAF can be directly passed to the model for the next model integration. The online mode eliminates the need for

133 intermediate steps and improves efficiency. Thirdly, the online mode is controlled by a main program, which allows for efficient

134 use of several processors in the high-performance computing cluster. Conversely, in the offline mode, the PDAF and the model

135 are managed by distinct programs, often with fewer processors available for each program. Therefore, the online-mode PDAF

136 is used in this study.

137

138 PDAF-OMI, an extension of PDAF, provides I/O interfaces for multi-type observations, simplifying user observation handling

139 by offering generic PDAF-OMI core routines and independent user-supplied routines for each observational type. The user-

140 supplied routines, namely *init_dim_obs/init_dim_obs_l*, *obs_op*, and *localize_covar*, are responsible for reading and writing

141 multi-type observations, applying corresponding observation operators, and performing covariance localization, respectively.

142 The modules for all observation types are integrated into the *callback_obs_pdafomi*, allowing free combinations between

143 different observation types without interference and facilitating the collaborative DA for various aerosol chemical components.

144 PDAF-OMI was not applied in NAQPMS-PDAF v1.0. Consequently, NAQPMS-PDAF v1.0 cannot switch between different

145 observational type combinations, and users need to define complete routines for each observation type for the DA process,

146 resulting in more tedious code writing and higher computational costs in NAQPMS-PDAF v1.0.

147 **2.3 NAQPMS-PDAF v2.0**

148 **2.3.1 Structure of NAQPMS-PDAF v2.0**

149 Figure 1 illustrates the structure (left portion) and main workflow (right portion) of NAQPMS-PDAF v2.0. As described in the

150 left portion of Fig. 1, the observation part involves the integration of multi-type observations (the purple cuboid patterns) and

151 the utilization of PDAF-OMI. PDAF-OMI enables the simultaneous access and scheduling of multi-type and multi-source

152 observations by employing observational indices, thereby facilitating flexible combinations of observations. The ensemble

153 initial fields (the deep blue cuboid patterns) are crucial inputs for the numerical simulation of NAQPMS. The ensemble

154 forecast/background fields (the deep yellow cuboid patterns) are generated by perturbing emission species based on

155 hypothesized distributions (see Sect. 2.3.3) and performing physiochemical calculations in NAQPMS (the green rectangular

156 patterns). Then, chemical DA is performed by a novel hybrid localized nonlinear DA algorithm (LKNETF, see Sect. 2.3.4)

157 with an adaptive hybrid weight and an adaptive forgetting factor to generate analysis fields (the orange cuboid patterns) for

158 the next realization.
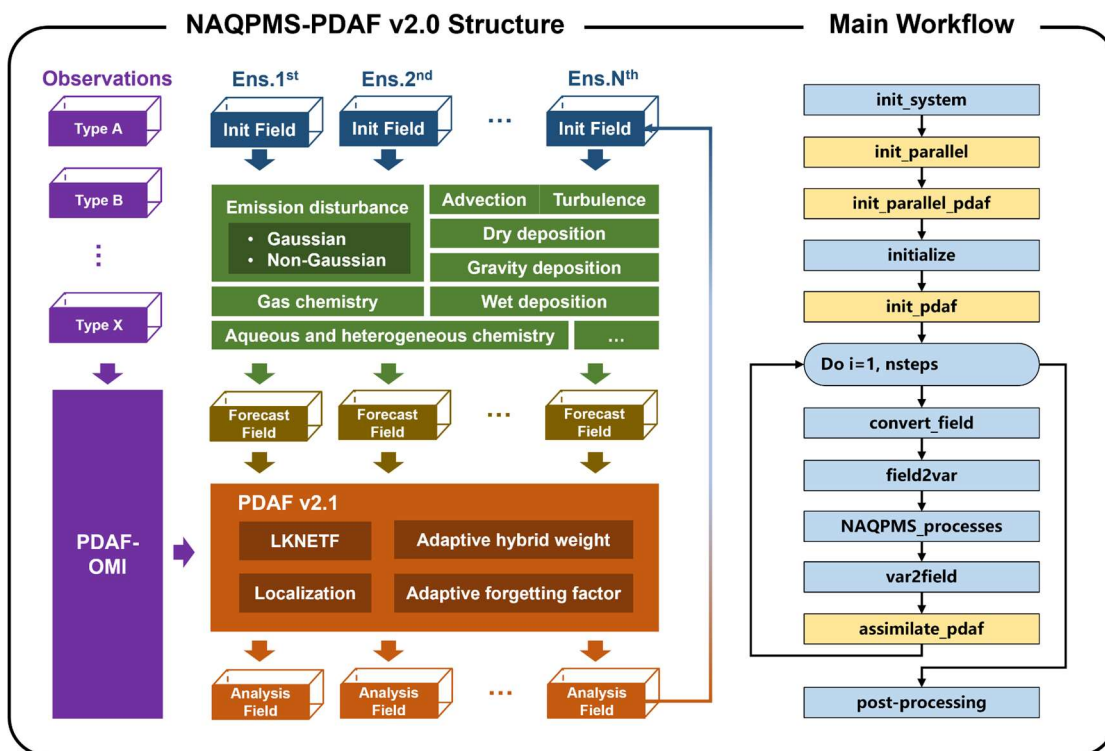
159

160 **Figure 1: The structure of NAQPMS-PDAF v2.0 (Left: the purple cuboid patterns represent the multi-type observations, the deep**

161 **blue cuboid patterns represent the initial fields, the deep yellow cuboid patterns represent the forecast or background fields, and the**

162 **orange cuboid patterns represent the analysis fields. Ens.1st represents the first ensemble member, and Ens.Nth represents the Nth**

163 **ensemble member. Right: the main workflow in NAQPMS-PDAF v2.0, blue rectangular patterns represent the modules in NAQPMS,**

164 **and yellow rectangular patterns represent the modules in PDAF).**

165 NAQPMS-PDAF v2.0 implements an online coupling between NAQPMS and PDAF v2.1 with OMI, utilizing a level-2

166 parallel computational framework. The description of level-2 parallel implementation was detailed in our previous work (Wang

167 et al., 2022). The online coupling ensures the continuous operation of model forecasts and assimilation analysis at each time

168 step, achieved by directly integrating PDAF routines into the prototype code of NAQPMS (the right portion of Fig. 1, the blue

169 represents NAQPMS main routines, while the yellow represents PDAF main routines). The level-2 parallel computational

170 framework, which utilizes the Message Passing Interface standard (MPI), facilitates concurrent processing and data exchange

171 among multiple ensemble members and parallel computation among model state matrixes within each ensemble member,

172 enhancing the efficiency of ensemble analysis and numerical model computations. For instance, the operation of twenty

173 ensemble members necessitates the execution of twenty model tasks, each of which performs integral calculations on a large

174 model grid. Twenty model tasks can be executed simultaneously at twenty computational nodes with sufficient computational

175 resources. Each model task can then perform parallel computation with multiple processors by splitting the large model grid

into multiple sub-grids. As illustrated in the right portion of Fig. 1, the workflow of NAQPMS-PDAF v2.0 is outlined as follows:

Step 1. *init_system* module initializes NAQPMS by defining all model state variables, allocating numerical matrixes, configuring parameters, I/O of meteorological fields, and emission input.

Step 2. *init_parallel* module initializes MPI (MPI_COMM_WORLD) and model communicator (MPI_COMM_MODEL), their number of processes, and the rank of a process, followed by *init_parallel_pdaf*, which initializes MPI communicators for the model tasks, filter tasks and the coupling between model and filter tasks.

Step 3. *initialize* module initializes the target field (such as $PM_{2.5}$ chemical components), such as their spatiotemporal dimensions (longitude, latitude, and time steps) and variable dimensions.

Step 4. *init_pdaf* module initializes PDAF variables, such as the local state dimension, global state dimension, and settings for analysis steps.

Step 5. Perform the time loop of forecast and analysis. The *convert_field* module is employed to match the matrix storage rule of the target field between NAQPMS and PDAF to ensure compatibility. The *field2var* module collects the analysis field/initial field and establishes a relationship between the initial field/analysis field and sub-variables in NAQPMS. Subsequently, the analysis field values are allocated to the corresponding NAQPMS sub-variables, and then the *NAQPMS_processes* module performs the forecast. After that, the *var2field* module, the inverse of the *field2var* module, assigns the NAQPMS sub-variables to the forecast field/background field. Finally, the *assimilate_pdaf* module assimilates the target field with observations to generate an analysis field for the next iteration.

Step 6. The *post-processing* module is responsible for finalizing NAPQMS-PDAF, data analysis, and DA evaluation.

2.3.2 Configurations

The meteorological field for NAQPMS is provided by the Weather Research and Forecasting model version 4.0 (WRFV4.0, https://www.mmm.ucar.edu/models/wrf). The initial-boundary conditions for WRF are obtained from NCEP GDAS Final Analysis (https://rda.ucar.edu/datasets/ds083.3/), with a horizontal resolution of 0.25°×0.25° and the temporal resolution of 6 hours, produced by the Global Data Assimilation System (GDAS). The land use data for WRF was updated by USGS's MCD12Q1 v006 in 2019 (https://lpdaac.usgs.gov/products/mcd12q1v006/) with 20 categories. Three nested model domains are conducted with the horizontal resolutions of 45 km in the East Asia region (domain1), 15 km in most areas of China except for the western area (domain2), and 5 km in the Northern China region (domain3, target research region). WRF and NAQPMS have 40 vertical layers with 27 layers within 2 km. The parameterization schemes for physical processes in WRF are shown in Table S2. The boundary condition input for NAQPMS is provided by the global chemistry transport Model for OZone And Related chemical Tracers version 2.4 (MOZART V2.4) (Horowitz et al., 2003). The anthropogenic emissions for NAQPMS are from Tsinghua University's 2016 Multi-resolution Emissions Inventory for China (MEIC, http://www.meicmodel.org/)

207 with a spatial resolution of 0.25°×0.25°, including residential sources, transportation sources, agricultural sources, industrial

208 sources, and power plant sources. The computational platform is the high-performance supercomputer subsystem cluster with

209 320 computation nodes, a total of 12,800 processors, and about 153 TB memory at the Big Data Cloud Service Infrastructure

210 Platform (BDCSIP), which meets the demand for high-performance parallel computing of NAQPMS-PDAF v2.0.

211

212 The model state variables include NH_4^+, SO_4^{2-}, NO_3^-, OC, EC, Na^+, Brown carbon, soil $PM_{2.5}$, soil PM_{10}, sea salt, fine dust,

213 coarse dust, SO_2, NO_2 and RH. As shown in Fig. 2, the model state has a 4-dimensional (4-D) structure with longitudinal

214 dimension (ix, 300 grids), latitudinal dimension (iy, 249 grids), variable dimension (ivar, 15), and vertical dimension (iz, 40

215 layers) in that order. The 4-D model state with 15 variables is converted to a 2-D state matrix in PDAF, the number of grids in

216 the horizontal axis direction is ix, and the number of grids in the vertical axis direction is iy*ivar*iz. Notably, the 2-D state

217 matrix coordinate index contains 3-D information for each variable to implement the horizontal and vertical domain

218 localization separately because the horizontal and vertical resolutions are not uniform. This structure has two advantages. First,

219 the parallel cutting of the horizontal axis enables the local domain to retain the full dimensional information (ix_p*iy*ivar*iz,

220 where ix_p is the longitudinal dimension of the local domain). Secondly, the localization in the local domain permits the

221 analysis to execute only within a small domain (ix_p*iy) when the length of the horizontal localization radius (R_s) is smaller

222 than iy, effectively reducing the influence of spurious correlations between different state variables. In this study, we set the

223 horizontal and vertical domain localization radius to 200 km (40 grids) and 1 layer. Besides, we further implemented the

224 observation localization to consider the influence of distance between analysis grid and observational grid (see Sect. 2.3.4). To

225 minimize computational complexity, the observation errors were assumed to be spatially isotropic, with 0.40 μg/m³, 1.00 μg/m³,

226 0.50 μg/m³, 3.00 μg/m³, and 0.50 μg/m³ for NH_4^+, SO_4^{2-}, NO_3^-, OC and EC, respectively.
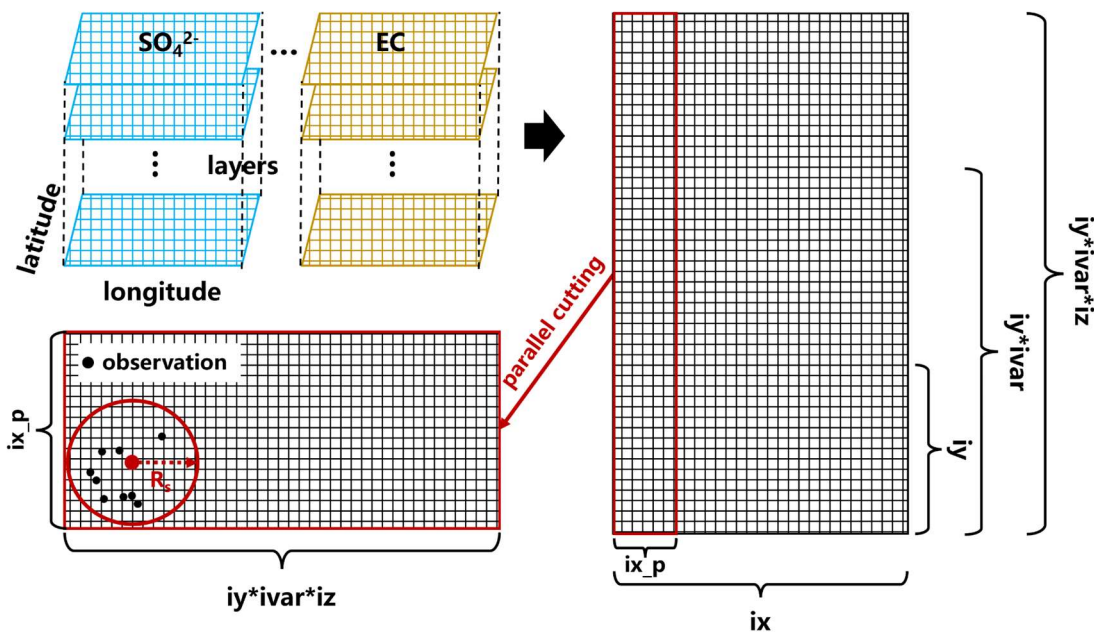
227

228 **Figure 2: The structure of state variables in NAQPMS-PDAF v2.0.**

2.3.3 Generation of ensemble members

In ensemble DA, ensemble members interpret the uncertainty of the model or system, characterized by BEC, which significantly impacts the DA performance (Dai et al., 2014). For CTMs, emission input directly influences the chemical calculation and substantially contributes to the uncertainty. Perturbing emission input can effectively represent the uncertainty in aerosol emissions and enhance the consistency of ensemble error spread, thereby improving aerosol DA (Huang et al., 2023). CTMs are nonlinear, and model state errors are non-Gaussian distributions. To obtain non-Gaussian error distributions, we followed the Kong et al. (2021) method to assume that the emission errors are spatially correlated by an isotropic correlation model with a decorrelation length of 150 km and generate perturbation coefficient matrixes with the same Gaussian distribution as the emission species, which are subsequently transformed into non-Gaussian distribution matrixes through non-Gaussian process generation v1.2 (Cheynet, 2024).

The target $PM_{2.5}$ chemical components are NH_4^+, SO_4^{2-}, NO_3^-, OC, and EC. The perturbed emission species that can directly or indirectly affect the component concentration calculations include SO_2, NO_x, VOC_s, NH_3, CO, PM_{10}, $PM_{2.5}$, EC, and OC, with the corresponding uncertainties (δ) listed in Table 1. As shown in Eq. (1), the original emission input matrix (E_p) is multiplied by the corresponding perturbation coefficient matrix (θ_i) to generate the perturbed emission input matrix (E_i) for each emission species. The calculation of the perturbation coefficient matrix (θ_i) is followed by Eq. (2)-(3). Firstly, N two-dimensional pseudorandom perturbation fields (P_i) are created using Evensen's method (Evensen, 1994). The uncertainties (δ) of the emission species are incorporated into the two-dimensional pseudorandom perturbation fields (P_i) to obtain the final perturbation coefficient matrixes (θ_i). Finally, the Gaussian-distribution perturbation coefficient matrixes (θ_i) were transformed into non-Gaussian distribution coefficient matrixes with a given target skewness (set to 1) and kurtosis (set to 6) by non-Gaussian process generation v1.2, which employs the Moment Based Hermite Transformation Model and a cubic transformation.

Table 1: The uncertainties of emission species in NAQPMS-PDAF v2.0

Species	SO_2	NO_x	VOC_s	NH_3	CO	PM_{10}	$PM_{2.5}$	EC	OC
Uncertainty δ	2.00	0.31	0.68	0.53	0.70	1.32	1.30	2.08	2.58

$$E_i = E_p \times \theta_i, i = 1,2,\dots,N \ , \tag{1}$$

$$\ln \theta_{o_i} = \left(\frac{(P_i - \frac{1}{N} \times \Sigma_{i=1}^N P_i)}{\sqrt{\frac{1}{N} \times \Sigma_{i=1}^N (P_i - \frac{1}{N} \times \Sigma_{i=1}^N P_i)^2}} - \frac{1}{2} \times \ln(1 + \delta^2) \right) \times \sqrt{\ln(1 + \delta^2)} \ , \tag{2}$$

$$\theta_i = \frac{\left(\theta_{o_i} - \frac{1}{N} \times \Sigma_{i=1}^N \theta_{o_i} \right)}{\sqrt{\frac{1}{N} \times \Sigma_{i=1}^N \left(\theta_{o_i} - \frac{1}{N} \times \Sigma_{i=1}^N \theta_{o_i} \right)^2}} \times \left(\frac{1}{N} \times \Sigma_{i=1}^N \theta_{o_i} \right) \times \delta + \frac{1}{N} \times \Sigma_{i=1}^N \theta_{o_i} \ , \tag{3}$$

Notably, all matrix operations involved are Schur Products. Where E_i denotes the ith ensemble perturbed emission input matrix, E_p indicates the original unperturbed emission input matrix and θ_i represents the ith ensemble perturbation

257 coefficient matrix. θ_{o_i} is the ith ensemble original perturbation coefficient matrix, which is obtained by mathematical

258 transformation of the ith ensemble pseudorandom perturbation matrix P_i, including standardization, scaling by uncertainty (δ),

259 and logarithm.

2.3.4 Hybrid nonlinear DA algorithm with adaptive forgetting factor

261 To thoroughly integrate the stability of EnKFs with the nonlinearity of nonlinear filters and be ideal for the nonlinear and non-

262 Gaussian-distribution situations, the hybrid LKNETF is used in this study. This section reviews the algorithms of LETKF,

263 LNETF, and their combination (LKNETF).

264

265 ETKF, a deterministic filter in EnKFs, efficiently obtains analysis samples using a transformation matrix and the square root

266 of the forecast error covariance (Bishop et al., 2001). In contrast to stochastic filters in EnKFs, ETKF prevents underestimation

267 of the analysis error covariance resulting from the random observation perturbations. And it is particularly applicable in

268 situations with small ensemble sizes (Lawson and Hansen, 2004). The realization of ETKF can be divided into the forecast

269 and analysis steps.

270

271 In the forecast step, the forecast state vector ($\mathbf{x}_t^f$) at t is generated by numerical model ($\mathbf{M}$) integration of the analysis state

272 vector ($\mathbf{x}_{t-1}^a$) at t-1. The forecast error covariance matrix ($\mathbf{P}_t^f$) can be calculated by the perturbation of the forecast ensemble

273 ($\mathbf{X}_t^{f'}$).

274 $\mathbf{x}_t^f = \mathbf{M}(\mathbf{x}_{t-1}^a), \mathbf{X}_t^f = [\mathbf{x}_{1_t}^f, \mathbf{x}_{2_t}^f, \dots, \mathbf{x}_{K_t}^f]$,   (4)

275 $\mathbf{P}_t^f = \mathbf{X}_t^{f'}\mathbf{X}_t^{f'^T}$,   (5)

276 Where $\mathbf{X}_t^f$ is the forecast ensemble at t, and K is the number of ensemble members. $\mathbf{X}_t^{f'}$ is the perturbation of the forecast

277 ensemble at t, calculated by $\mathbf{X}_t^f$ and the forecast ensemble mean $\overline{\mathbf{X}_t^f}$ at t.

278

279 In the analysis step, the forecast error covariance matrix ($\mathbf{P}_t^f$) at t is transformed to the analysis error covariance matrix ($\mathbf{P}_t^a$) at

280 t by a transform matrix ($\mathbf{T}$).

281 $\mathbf{P}_t^a = \mathbf{X}_t^{f'}\mathbf{T}\mathbf{X}_t^{f'^T}$,   (6)

282 The transform matrix ($\mathbf{T}$) is defined as follows and can be decomposed to a left singular vector matrix ($\mathbf{U}$), a singular value

283 matrix ($\mathbf{S}$), and a right singular vector matrix ($\mathbf{V}$) through the singular value decomposition.

284 $\mathbf{T}^{-1} = \rho_{adaptive}(K-1)\mathbf{I} + (\mathbf{H}\mathbf{X}_t^{f'})^T(\mathbf{L} \cdot \mathbf{R}^{-1})\mathbf{H}\mathbf{X}_t^{f'} = \mathbf{U}\mathbf{S}\mathbf{V}$,   (7)

285 $$\rho_{adaptive} = \frac{\sigma_{ens}^2}{\sigma_{resid}^2 - \sigma_{obs}^2} \ , \tag{8}$$

286 Where $\rho_{adaptive}$ is an adaptive forgetting factor used for the inflation of error covariance estimation (the initial $\rho_{adaptive}$ is

287 set to 0.9 in this study). σ_{ens}^2 is the mean ensemble variance, σ_{resid}^2 is mean of observation-minus-forecast residual, σ_{obs}^2 is

288 mean observation variance. **I** is the identity matrix. **H** is the observation operator. **L** is the localization matrix, a weight

289 matrix calculated by the 5th-order polynomial (Nerger, 2015), implemented in LETKF for observation localization analysis to

290 avoid observational spurious correlation and filter divergence effectively (Hunt et al., 2007). **R** is the observation error

291 covariance matrix.

292

293 The analysis state vector ($\mathbf{x}_t^a$) at t is calculated by the forecast state vector ($\mathbf{x}_t^f$) at t, the perturbation of the forecast ensemble

294 ($\mathbf{X}_t^{f'}$) at t and a weight vector (**w**).

295 $$\mathbf{x}_t^a = \mathbf{x}_t^f + \mathbf{X}_t^{f'}\mathbf{w} \ , \tag{9}$$

296 The weight vector (**w**) is given by the following equation.

297 $$\mathbf{w} = \mathbf{T}(\mathbf{H}\mathbf{X}_t^{f'})^\mathrm{T}(\mathbf{L} \cdot \mathbf{R}^{-1})(\mathbf{y} - \mathbf{H}\mathbf{x}_t^f) \ , \tag{10}$$

298 Where **y** is observations.

299

300 The analysis ensemble ($\mathbf{X}_t^a$) at t can be obtained by forecast ensemble mean ($\overline{\mathbf{X}_t^f}$) at t, the perturbation of the forecast ensemble

301 ($\mathbf{X}_t^{f'}$) at t and a transform matrix (**C**) represented by the symmetric square root of **T**.

302 $$\mathbf{X}_t^a = \overline{\mathbf{X}_t^f} + \sqrt{K-1}\mathbf{X}_t^{f'}\mathbf{C} \ , \tag{11}$$

303 The transform matrix (**C**) is calculated as follows.

304 $$\mathbf{C} = \mathbf{U}\mathbf{S}^{-1/2}\mathbf{U}^\mathrm{T} \ , \tag{12}$$

305 NETF is a 2nd-order exact ensemble square root filter effectively applied to the nonlinear and non-Gaussian DA (Tödter and

306 Ahrens, 2015). Like PF, NETF indirectly updates the model state by using observations to affect the weights of the prior

307 ensemble. However, PF and NETF differ in the sampling method. PF utilizes the Monte Carlo and Bayesian approaches to

308 calculate particle weights based on observations, which are then used to generate the analysis ensemble by weighting the

309 resampling forecast ensemble. In high-dimensional systems, as the DA progresses, the weight differences of particles increase,

310 with most particles having weights close to 0, leading to filter degeneration. In contrast, NETF generates the analysis ensemble

311 through a deterministic matrix square root transformation of the forecast ensemble, where the mean and covariance matrix of

312 the analysis ensemble match the weighted values in PF (as shown in Eq. (13)-(14)). Due to the similarity between NETF and

313 ETKF, the localization can be implemented in NETF (LNETF) (Tödter et al., 2016).

314      $\bar{\mathbf{x}}^a = \frac{1}{K}\sum_{i=1}^{K}\mathbf{x}_i{}^a = \frac{1}{K}\sum_{i=1}^{K}w_i\mathbf{x}_i{}^f$,   (13)

315   Where $\bar{\mathbf{x}}^a$ is the analysis state vector mean, K is the number of ensemble members, $\mathbf{x}_i{}^a$ is the ith analysis state vector, w_i is

316   the ith particle weight vector in PF, which is calculated by the Bayesian method $w_i = p(\mathbf{y}|\mathbf{x}_i{}^f)/p(\mathbf{y})$, $\mathbf{y}$ is the observations,

317      $\mathbf{x}_i{}^f$ is the ith forecast state vector.

318      $\mathbf{P}^a = \frac{1}{K-1}\sum_{i=1}^{K}(\mathbf{x}_i{}^a - \bar{\mathbf{x}}^a)(\mathbf{x}_i{}^a - \bar{\mathbf{x}}^a)^T = \sum_{i=K}^{K}w_i(\mathbf{x}_i{}^f - \bar{\mathbf{x}}^f)(\mathbf{x}_i{}^f - \bar{\mathbf{x}}^f)^T$,   (14)

319   Where $\mathbf{P}^a$ is the error covariance matrix of the analysis ensemble, calculated by the perturbation of the analysis ensemble.

320   In NETF, $\mathbf{A}$ performs as a transform matrix like the transform matrix ($\mathbf{T}$) in ETKF, which can be obtained from the weight

321   matrix ($\mathbf{w}$).

322      $\mathbf{P}^a = \mathbf{X}^{f\prime}\mathbf{A}\mathbf{X}^{f\prime T}$,   (15)

323      $\mathbf{A}^{1/2} = (\mathbf{W} - \mathbf{w}\mathbf{w}^T)^{1/2} = \mathbf{V}\mathbf{D}^{1/2}\mathbf{V}^T$,   (16)

324   Where the matrix $\mathbf{W} \equiv \text{diag}(\mathbf{w})$ is defined as a diagonal matrix created from the weight matrix ($\mathbf{w}$). $\mathbf{A}$ can be decomposed

325   ($\mathbf{A} = \mathbf{V}\mathbf{D}\mathbf{V}^T$) by a singular value decomposition as it is a real, symmetric, positive semidefinite matrix. $\mathbf{V}$ is the orthogonal

326   matrix, and $\mathbf{D}$ is a diagonal matrix.

327

328   Then, the perturbation of the analysis ensemble ($\mathbf{X}^{a\prime}$) and the analysis ensemble ($\mathbf{X}^a$) can be obtained by applying the square

329   root of $\mathbf{A}$ as a transform matrix.

330      $\mathbf{X}^{a\prime} = \sqrt{K}\mathbf{X}^{f\prime}\mathbf{A}^{1/2}$,   (17)

331      $\mathbf{X}^a = \bar{\mathbf{X}}^f + \mathbf{X}^{f\prime}(\bar{\mathbf{W}} + \sqrt{K}\mathbf{A}^{1/2})$,   (18)

332   LKNETF combines the LETKF and LNETF through a hybrid weight γ to perform better in systems with different non-

333   linearity degrees and implement in situations with smaller ensemble sizes (Nerger, 2022). When γ approaches 1, the analysis

334   increment ($\Delta\mathbf{X}_{LETKF}$) computed by LETKF becomes more significant and appropriate for linear systems with Gaussian

335   distributions. Conversely, when γ approaches 0, the analysis increment ($\Delta\mathbf{X}_{LNETF}$) computed by LNETF becomes more

336   significant and appropriate for non-linear systems with non-Gaussian distributions. The one-step update scheme is used in this

337   study.

338      $\mathbf{X}_{HSync}^a = \bar{\mathbf{X}^f} + (1 - \gamma)\Delta\mathbf{X}_{LNETF} + \gamma\Delta\mathbf{X}_{LETKF}$,   (19)

2.4 Data

2.4.1 Observation

The one-month (February 2022) hourly mass concentration observations of five $PM_{2.5}$ chemical components (NH_4^+, SO_4^{2-}, NO_3^-, OC, and EC) from 33 ground-based sites in Northern China and surrounding areas were collected for this work (Fig. 3). Out of the 33 sites, 24 (DA sites) were utilized for DA and internal validation, and the remaining 9 (VE sites) were used for independent verification to assess the influence of DA sites on neighboring areas. These sites were divided using the K-means clustering algorithm (Lloyd, 1982; Arthur and Vassilvitskii, 2007). The supplement provides a detailed description (Text S1). $PM_{2.5}$ hourly observations from the China National Environmental Monitoring Centre (CNEMC, http://www.cnemc.cn/) were employed to assess the overall mass concentration of $PM_{2.5}$ chemical components in NAQPMS-PDAF v2.0. Due to incomplete spatial overlap between the $PM_{2.5}$ sites and the chemical component sites, the $PM_{2.5}$ sites were selected based on the closest Euclidean distance between $PM_{2.5}$ sites and chemical component sites.
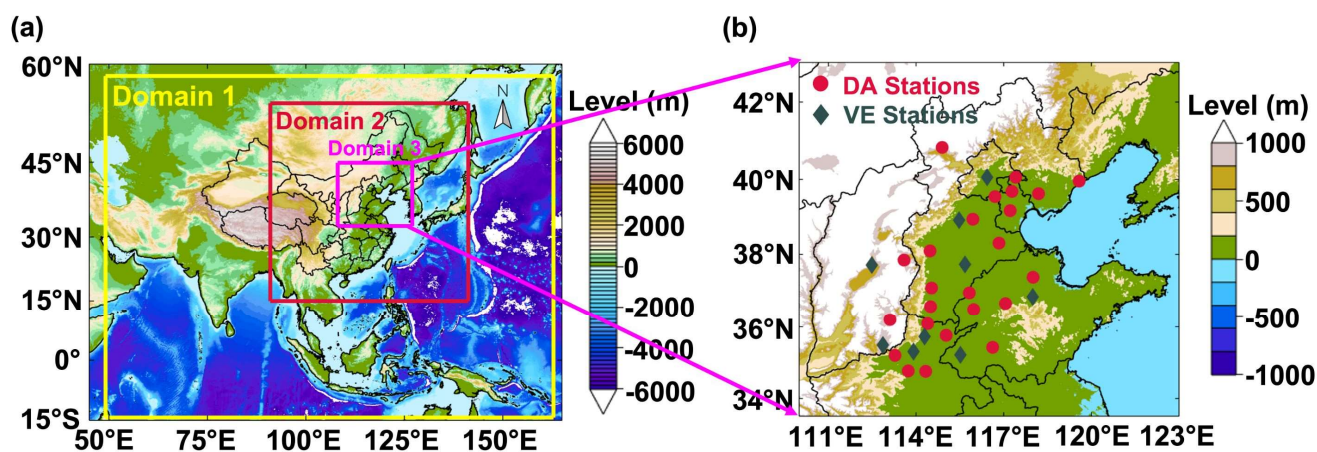
Figure 3: The model domains in WRF simulation (a) and the location of observations (b). Domain 3 in (a) is the target area of this study. Twenty-four red sites in (b) represent the sites for data assimilation, and nine green sites in (b) represent the sites for spatial independent validation. The topographic dataset is from the ETOPO1 1 arc-minute Global Relief Model, taken from the National Geophysical Data Center (Amante and Eakins, 2009).

2.4.2 Global reanalysis dataset

The global reanalysis datasets of $PM_{2.5}$ chemical components in February 2022 were obtained from the Copernicus Atmosphere Monitoring Service ReAnalysis (CAMSRA, 0.75°×0.75°) (Inness et al., 2019) and the Modern-Era Retrospective analysis for Research and Applications, Version 2 (MERRA-2, 0.5°×0.625°) (Randles et al., 2017) to compare with reanalysis dataset generated by NAQPMS-PDAF v2.0. For the data consistency, the global reanalysis surface grid data located in the observation sites of $PM_{2.5}$ chemical component were extracted through the k-nearest neighbor search method (Friedman et al., 1977), which can efficiently match grid points and observation sites based on longitude and latitude data and Euclidean distances. Our 3-hourly NAQPMS-PDAF v2.0 output of NO_3^- and NH_4^+ were extracted to compare with the CAMSRA dataset, and hourly NAQPMS-PDAF v2.0 output of SO_4^{2-}, OC, and EC were extracted to compare with MERRA-2 M2T1NXAER dataset.

2.5 Experimental setting and evaluation method

In our study, four tests were conducted to evaluate the performance of NAQPMS-PDAF v2.0 with hourly observations of five $PM_{2.5}$ chemical components, including (1) the dependence on ensemble size and assimilation frequency, (2) the interpretation ability on mass concentration and spatiotemporal characteristics, (3) the quality of output data compared to other reanalysis datasets, and (4) the uncertainty in ensemble assimilation. In practice, the ratio of ensemble size to the number of processes with 1:50 in high-performance computers was the optimal parallel scheme to balance computing efficiency and computing resources (Wang et al., 2022).

All the tests were run in NAQPMS-PDAF v2.0 after a spin-up experiment with 24 timesteps from 00:00 to 23:00 (LST) on February 1st, 2022. (1) For the first test, we assimilated the hourly observations of five $PM_{2.5}$ chemical components from all sites with 48 timesteps from 00:00 (LST) on February 2nd to 23:00 (LST) on February 3rd, 2022. In the first scenario, we controlled a fixed assimilation frequency of 1 hour and changed the ensemble size to 2, 5, 10, 15, 20, 30, 40, and 50. In the second scenario, we controlled a fixed ensemble size of 20 and changed the assimilation frequency to 1 hour, 2 hours, 3 hours, 4 hours, 5 hours, 6 hours, 8 hours, and 12 hours. (2) For the second test, we set an ensemble size of 20 and an assimilation frequency of 1 h and assimilated the hourly observations of five $PM_{2.5}$ chemical components from DA sites with 648 timesteps from 00:00 (LST) on February 2nd to 23:00 (LST) on February 28th, 2022. We also conducted a free running (FR) experiment without assimilation in the same period for comparison. (3) For the third test, we followed the settings in the second test but assimilated the observation from all sites to generate a high-quality reanalysis dataset of five $PM_{2.5}$ chemical components. (4) The final test was analogous to the first test but with a distinct scenario designed to examine the influence of ensemble perturbation on ensemble assimilation. From Table 2, we fixed species uncertainty (M4 setting) with five distribution types in the first scenario and fixed distribution type (T2 setting) with five SO_2 uncertainties in the second.

Table 2: The experiment settings for emission perturbation

Experiment	Distribution (Fixed species uncertainty)
T1	Gaussian
T2	Non-Gaussian (m3=1, m4=6)
T3	Non-Gaussian (m3=-1, m4=6)
T4	Non-Gaussian (m3=1, m4=12)
T5	Non-Gaussian (m3=-1, m4=12)
	SO_2 uncertainty (Fixed distribution)
M1	12%
M2	50%
M3	100%
M4	200%
M5	300%

387   We used the Continuous Ranked Probability Score (CRPS) to evaluate ensemble size dependency, which measures the

388   consistency between ensemble forecast distribution and corresponding observations (Jolliffe and Stephenson, 2012). The

389   calculation rules are referred to in Hersbach's study (Hersbach, 2000). Besides, four common statistical indicators, the Pearson

390   correlation coefficient (CORR), root mean square error (RMSE), mean absolute error (MAE), and coefficient of determination

391   (R^2), were used to assess the DA system performance in interpreting $PM_{2.5}$ chemical components (SO_4^{2-}, NO_3^-, NH_4^+, OC, and

392   EC). The CORR measures the correlation between the system outputs and corresponding observations, the RMSE and MAE

393   indicate the overall system accuracy, and the R^2 reflects the proportion of variability in the observations explained by the

394   assimilation system.

3 Results and discussion

3.1 The Dependence on Ensemble Size and Assimilation Frequency for Five Components

397   Ensemble size is a crucial parameter in ensemble assimilation, determining the model state's uncertainty range. A larger

398   ensemble size more accurately represents the error distribution of state variables but requires considerable computing resources

399   and time, especially for high-dimension systems. A smaller ensemble size can easily lead to underestimating the error

400   covariance matrix, especially for the fine-resolution model (Kong et al., 2021). Thus, identifying an appropriate ensemble size

401   to balance computational efficiency and accuracy is the primary step in ensemble DA. A prior study (NAQPMS-PDAF v1.0)

402   only evaluated the correlation between ensemble size and parallel efficiency and concluded that the ratio of ensemble size to

403   high-performance computing processors was 1:50 (Wang et al., 2022), while the impact of ensemble size on the accuracy and

404   computational efficiency was neglected. This study assessed the NAQPMS-PDAF v2.0 dependency on ensemble size through

405   three statistical indicators (CRPS, RMSE, and CORR). Figure 4 shows the mean CRPS, RMSE, and CORR values and the

406   statistical averages of the elapsed time over 48 timesteps with the ensemble sizes of 2, 5, 10, 15, 20, 30, 40, and 50.

408   From Fig. 4a, when the ensemble size is at its minimum level of 2, the mean CRPS values of the five $PM_{2.5}$ chemical

409   components are more significant, with NO_3^- exhibiting the most considerable difference between the simulation distribution

410   and observations (more than 4). With each increase in ensemble size, the mean CRPS values of the five chemical components

411   progressively reduce and eventually reach convergence when the ensemble size is 10, implying that a hybrid nonlinear filter

412   can maintain high accuracy and reliability in ensemble assimilation with an ensemble size that is smaller than the traditional

413   minimum of 20 ensemble members, as observed in prior ensemble assimilation studies (Constantinescu et al., 2007; Miyazaki

414   et al., 2012; Schwartz et al., 2014; Rubin et al., 2017; Kong et al., 2021; Tsikerdekis et al., 2021; Wang et al., 2022), including

415   NAQPMS-PDAF v1.0. The mean CRPS value of EC is the lowest among the five chemical components, indicating the highest

416   accuracy and reliability of EC ensemble DA. The performance of other components is similar. Like CRPS values, the values

417   of RMSE and CORR decrease and increase, respectively, as the ensemble size increases, and convergence begins to occur

418   when the ensemble size is 10 (Fig. 4b and c). Compared with other chemical components, the CORR value of SO_4^{2-} is

419   significantly lower, less than 0.8, possibly due to its estimated background field error covariance driven by the inadequate

420   ensemble perturbations. Therefore, in the Discussion section, we discuss the uncertainties of ensemble perturbations.
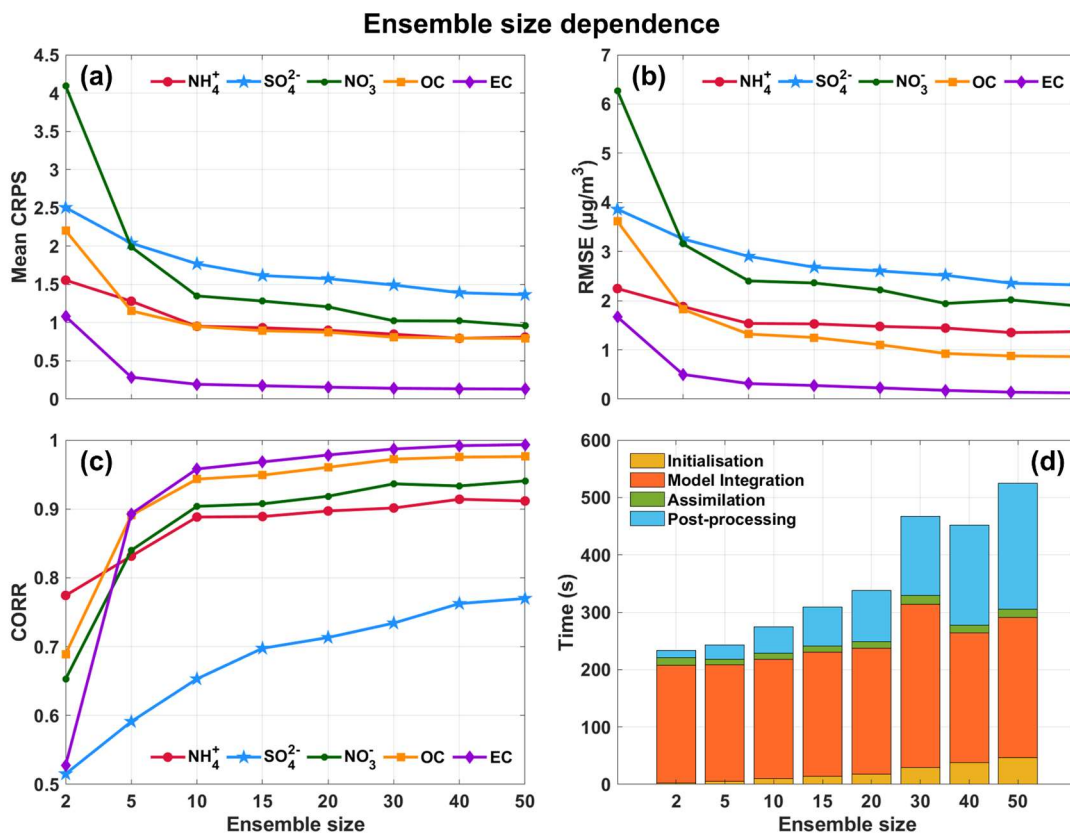
421

422   **Figure 4: Assessment of ensemble size dependency based on mean continuous ranked probability score (CRPS) (a), root mean square**

423   **error (RMSE) (b), correlation coefficient (CORR) (c), and time (d).**

424   Figure 4d shows the time required for the four processes of ensemble assimilation under different ensemble sizes, including

425   initialization, model integration, assimilation, and post-processing. The model integration process in NAQPMS-PDAF v2.0

426   takes the longest, followed by post-processing, initialization, and assimilation. The required time for initialization and post-

427   processing increases with increasing ensemble size, while for model integration and assimilation, except for ensemble size 30,

428   the required time is the same under different ensemble sizes. Generally, the time needed for ensemble sizes of 30-50 is

429   considerably higher than that for smaller ones. Although convergence occurs with an ensemble size of 10, our work illustrates

430   a similar time required between ensemble sizes 10 and 20. Consequently, we selected an ensemble size of 20 to ensure optimal

431   performance of NAQPMS-PDAF v2.0, considering both assimilation efficiency and accuracy.

432

433   The assimilation frequency is the interval at which observational data is introduced into the DA system, directly affecting the

434   practical assimilation data volume and computation cost. High-frequency DA with high-quality observations is crucial for

435   improving numerical simulations and forecasts (Liu et al., 2021). Figure 5 demonstrates that the MAE values of the five

436 chemical components analysis fields range from 0.02 to 0.12 µg/m³, RMSE values range from 0.23 to 2.61 µg/m³, and CORR

437 values range from 0.71 to 0.98 at a 1-hour assimilation time interval, which is significantly better than the statistical indicators

438 at lower assimilation frequencies. Even at a 2-hour assimilation frequency, the assimilation effect drops sharply compared to

439 the 1-hour interval, especially for NO_3^-, OC, and EC. The values of MAE and RMSE increase by 2.6-5.82 µg/m³ and 4.72-

440 9.57 µg/m³, respectively, and the CORR values decrease by 0.27-0.81. Gradual increasing trends in MAE and RMSE values

441 and a slight decreasing trend in CORR values are observed as assimilation frequency decreases from the 2-hour interval.

442 Therefore, the fast-updating assimilation with a 1-hour interval significantly improves the NAQPMS simulation. For the

443 forecasting field (Fig. S2), the low sensitivity of state variables to assimilation frequency suggests that NAQPMS-PDAF v2.0

444 can appropriately reduce assimilation frequency during the actual forecasting phase, lowering the demand for high temporal

445 resolution observations and computational resources.
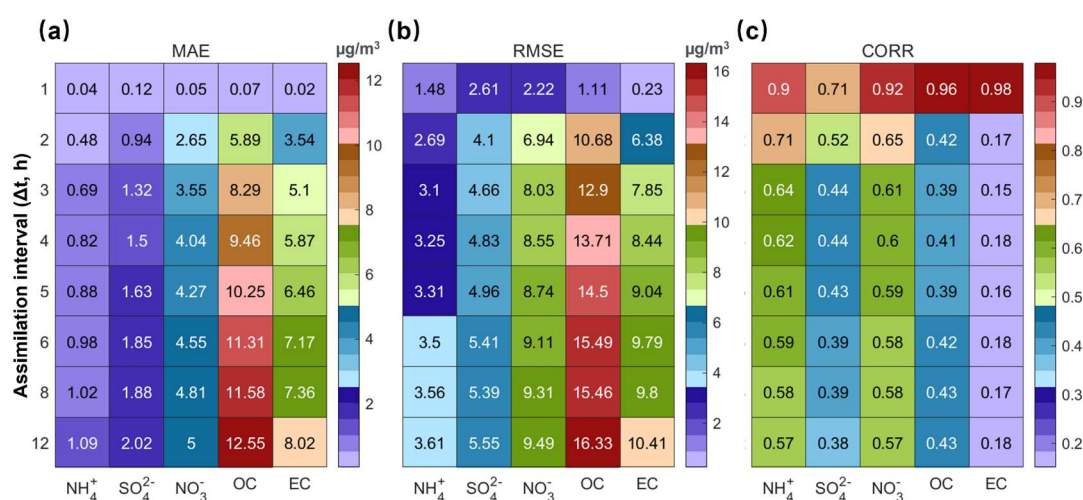
446
447 **Figure 5: Assessment of assimilation interval dependency based on mean absolute error (MAE) (a), root mean square error (RMSE)**
448 **(b), and correlation coefficient (CORR) (c) at the analysis step.**

449 **3.2 Evaluation of NAQPMS-PDAF v2.0 performance**

450 **3.2.1 Overall validation of DA results**

451 We conducted a control experiment (free-running field, FR) without any DA and a DA experiment. This section verified the

452 forecast field (FOR) and analysis field (ANA) at 24 DA sites and 9 VE sites, respectively. Figure 6 shows the scatter distribution

453 of observations and simulations at DA sites. For FR (Fig. 6a1-a5), five chemical components have CORR values ranging from

454 0.32 to 0.56, and R^2 values do not exceed 0.3, indicating poor consistency between observations and simulations. In detail, the

455 simulated mass concentrations of SO_4^{2-}, OC, and EC are significantly overestimated, while the simulated concentrations of

456 NH_4^+ and NO_3^- are underestimated. OC has the most significant error, with an RMSE value of 25.84 µg/m³ and an MAE value

457 of 19.41 µg/m³. Besides, the error distributions of SO_4^{2-}, NO_3^- and NH_4^+ are close to a symmetric distribution with a mean

458 value of 0, while the error distributions of OC and EC are skewed to the left from the mean value of 0 (Fig. 7a1-a5), showing

459 the relatively better simulations in SO_4^{2-}, NO_3^- and NH_4^+ than in OC and EC. Overall, NAQPMS cannot interpret the mass

concentrations of the five chemical components with significant errors, mainly due to the uncertainties in chemical mechanisms (Miao et al., 2020).
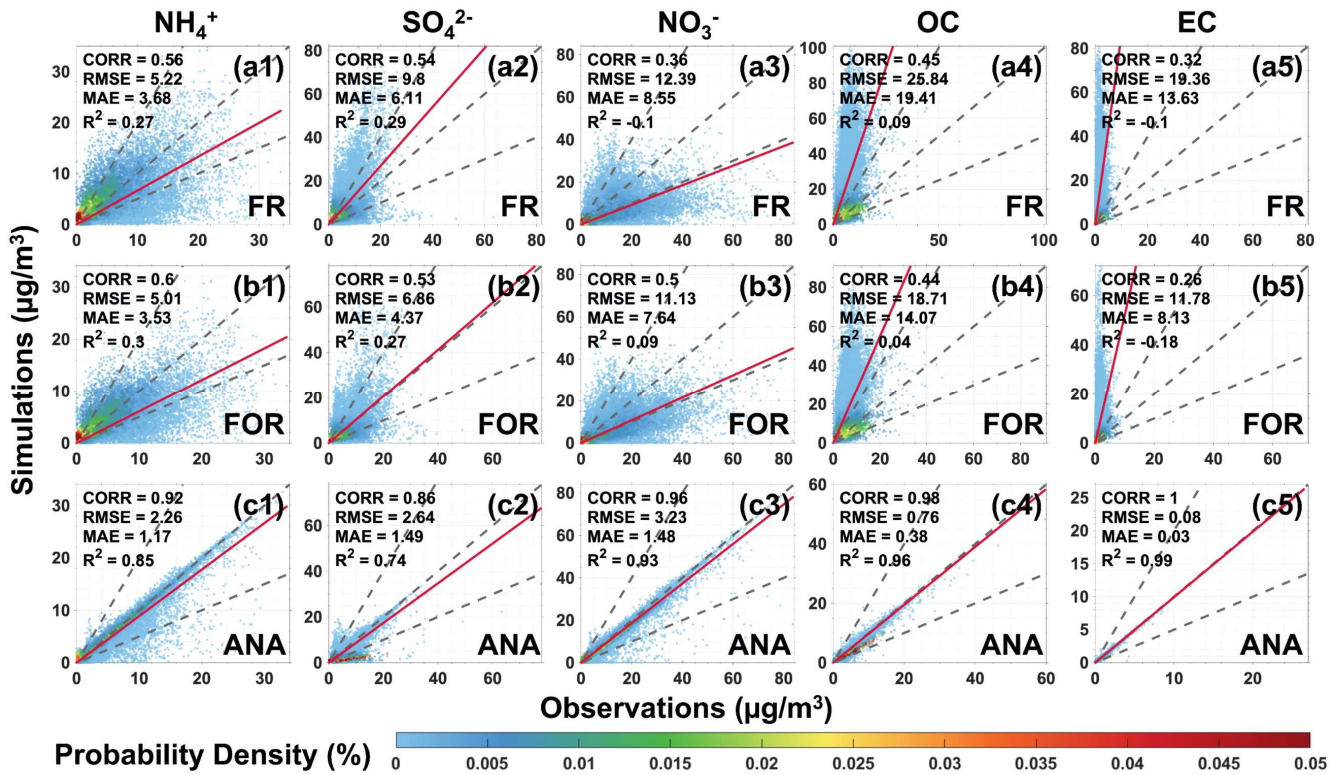
Figure 6: Scatterplots of the DA-site simulations versus the DA-site observations with probability density for the free-running field (FR, a1-a5), forecast field (FOR, b1-b5), and analysis field (ANA, c1-c5). The dotted gray lines represent the 2:1, 1:1, and 1:2 lines, and the solid red line represents the fitting regression line.
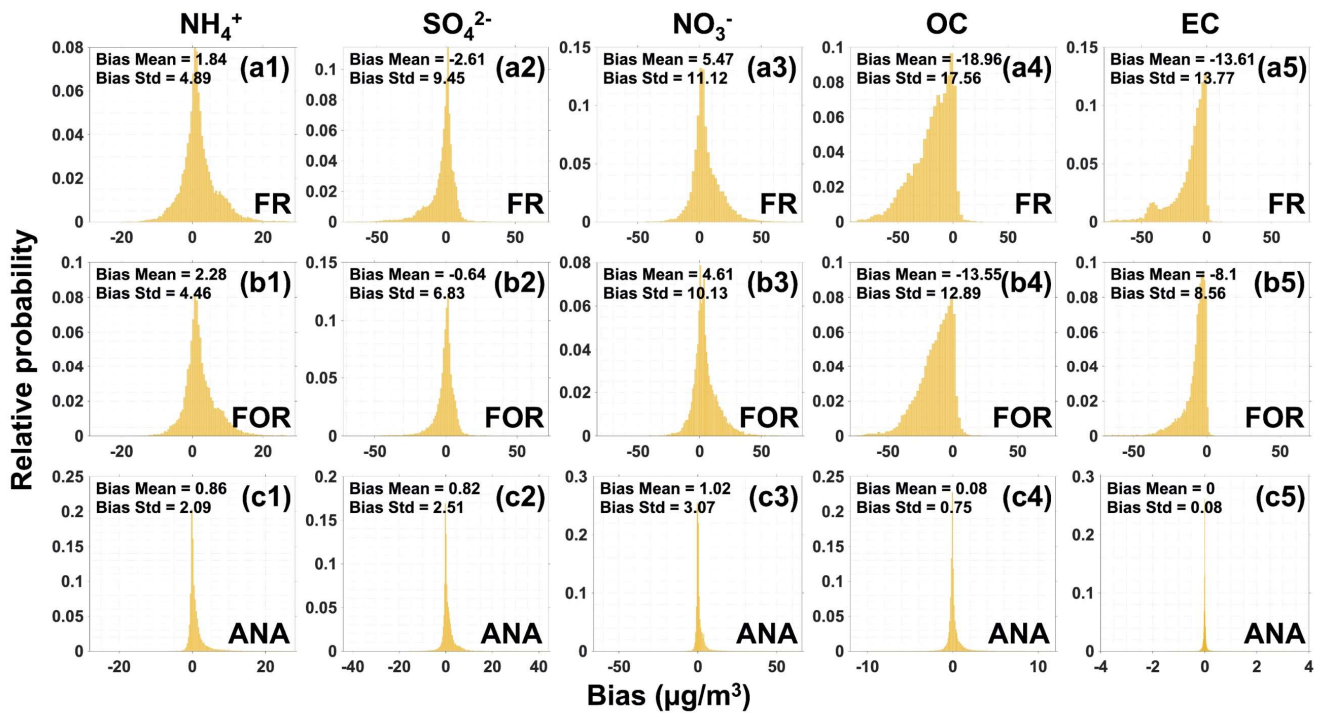
Figure 7: Probability distributions of bias between DA-site observations and DA-site simulations for the free-running field (FR, a1-a5), forecast field (FOR, b1-b5), and analysis field (ANA, c1-c5).

469   After DA, FOR shows a slight improvement with a slight increase in CORR and R^2 and a decrease in RMSE and MAE,

470   especially for NH_4^+ and NO_3^- (Fig. 6b1-b5). Although SO_4^{2-}, OC, and EC are significantly overestimated with a slight decrease

471   in CORR and R^2, the RMSE and MAE values decrease. Besides, the error distributions of the five chemical components are

472   concentrated at 0, and the overestimation of OC and EC has been improved compared to FR (Fig. 7b1-b5). These results

473   indicate that DA reduces the overall FOR errors in NAQPMS due to improved forecasting ability by obtaining optimal initial

474   fields. However, further improvements are necessary to address the NAQPMS uncertainties in emission sources,

475   meteorological input, and imperfect physiochemical mechanisms. For ANA (Fig. 6c1-c5), DA significantly improves the

476   simulations of the five chemical components, making the ANA consistent with the observations. The CORR values are not

477   less than 0.86, the RMSE and MAE values do not exceed 3.23 µg/m^3 and 1.49 µg/m^3, respectively, and the R^2 values are not

478   less than 0.74. Specifically, the CORR values for NO_3^-, OC, and EC are not less than 0.96, and the R^2 values are not less than

479   0.93. The error distributions of the five chemical components concentrate to 0 with the mean bias ranging from 0±0.08 µg/m^3

480   to 1.02±3.07 µg/m^3 (Fig. 7c1-c5). The results of VE sites show similar characteristics to the DA sites (Fig. S3 and S4).

481   Compared to FR, the overall errors of the FOR and ANA for the five chemical components decrease with a significant

482   improvement in ANA, showing that the CORR values of NH_4^+ and NO_3^- increase by 0.15 and 0.45, respectively, the R^2 values

483   of NH_4^+ and NO_3^- increase by 0.22 and 0.81, respectively, the RMSE values of OC and EC decrease by 21.77 µg/m^3 and 17.79

484   µg/m^3, respectively. Overall, the FOR and ANA errors decreased significantly. The ANA of the five chemical components at

485   DA sites is almost entirely consistent with the observations, indicating excellent DA performance.

486   **3.2.2 Assessment of temporal variation in chemical components**

487   The ensemble DA employs a cyclic updating process wherein the forecast and analysis steps are continuously completed at

488   each iteration (Evensen, 2003; Houtekamer and Zhang, 2016). In the forecast step, the ANA at the current time step serves as

489   the optimal initial field to advance the model integration and obtain the FOR at the next step. In the analysis step, the FOR at

490   the next time step provides background field information for the subsequent DA analysis to generate the ANA at the next time

491   step. The FOR and ANA interact with each other in the temporal dimension. Therefore, in this section, we assess the ability of

492   NAQPMS-PDAF v2.0 to interpret the temporal variations of the five chemical components. Figure 8 illustrates the time series

493   of the five chemical components at two representative sites, including a DA site in Tianjin City and a VE site in Heze City. For

494   the DA site (Fig. 8a), the temporal variations of NH_4^+ and NO_3^- in FR and FOR exhibit better agreement with the observed

495   temporal variations (OBS) than those of SO_4^{2-}, OC, and EC. However, NH_4^+ and NO_3^- mass concentrations are significantly

496   lower than the high-value mass concentrations observed on February 25th. The mass concentration of SO_4^{2-} in FR is greatly

497   overestimated during the periods of Feb. 8th-11th, Feb. 18th-19th, and Feb. 24th-25th. The mass concentrations of OC and EC in

498   FR are overestimated throughout February with substantial temporal fluctuations. Although the time series of SO_4^{2-}, OC, and

499   EC in FOR show some improvement, noticeable differences from the OBS are still apparent. After DA, the ANA time series

500   for the five chemical components align well with the OBS, indicating good consistency and accurate representation of temporal

501   characteristics, such as the NH_4NO_3 pollution captured on February 25th. Notably, the mass concentrations of SO_4^{2-}, NO_3^-, and

502   NH_4^+ peaked on Feb. 8th-11th and February 25th, indicating intensified atmospheric secondary chemical reactions primarily due

503   to neutralization reactions of acidic pollutants capturing NH_3. The temporal variations of NH_4^+ and NO_3^- are more similar

504   because atmospheric NO_3^- mainly exists as NH_4NO_3 rather than other metal nitrates, and NH_4NO_3 can form before the complete

505   neutralization of H_2SO_4 (Ge et al., 2017). The improvements at the VE site (Fig. 8b) are like those at the DA site, with the

506   ANA time series of the five chemical components showing closer agreement with the OBS, which suggests that the localization

507   analysis in DA effectively facilitates the propagation of observations within a specific spatial range and mitigates the

508   assimilation anomalies caused by spurious correlations from the distant sites (Hunt et al., 2007).
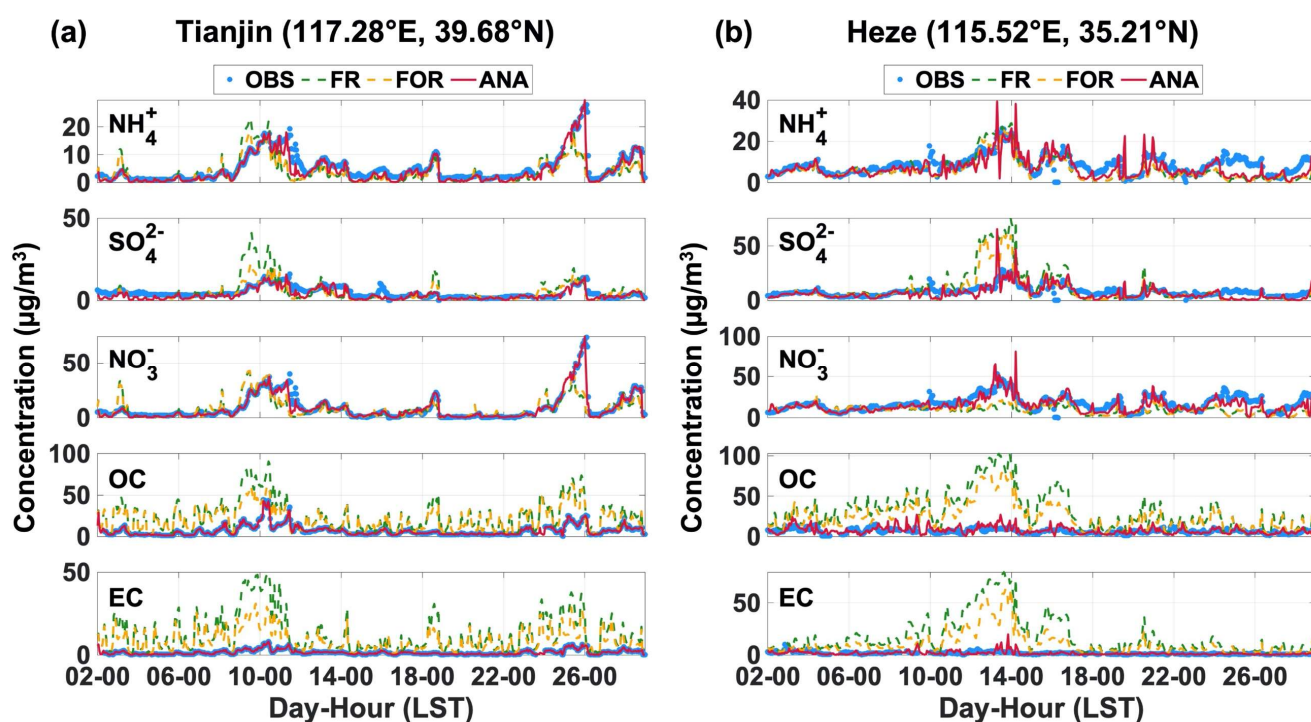
510   **Figure 8: Hourly variation of five PM₂.₅ chemical components in a representative DA site (a) and a representative VE site (b).**

511   NH_4^+, SO_4^{2-}, NO_3^-, OC, and EC are critical chemical components of $PM_{2.5}$, and the sum of their mass concentrations can be

512   approximated as the $PM_{2.5}$ mass concentration. We further assessed the simulation enhancement of $PM_{2.5}$ time series based on

513   ground-level $PM_{2.5}$ observations. Six representative sites were selected, including 3 DA sites (Fig. 9a1-a3) and 3 VE sites (Fig.

514   9b1-b3). The FR and FOR in DA and VE sites show significant overestimation and poor consistency with the OBS, mainly

515   due to the overestimation of OC and EC mass concentrations. Conversely, the $PM_{2.5}$ time series in ANA closely matches that

516   of the OBS, accurately capturing the actual variation of $PM_{2.5}$. In some specific instances, such as on February 26th at 00:00 in

517   Tianjin City and Langfang City, the peak value of ANA was lower than that of OBS, which could be attributed to the negligence

518   of other $PM_{2.5}$ components (such as mineral dust and sea salt) and the inconsistency in location between ground-level $PM_{2.5}$

519   observational sites and chemical components observational sites. Overall, the DA of chemical component observations

520 significantly enhanced the simulation of PM$_{2.5}$ time series in NAQPMS. Compared to the CORR values of FR and FOR, the

521 CORR values of ANA at the six representative sites increased by 13.64%-89.58% and 17.19%-75.00%, respectively, while the

522 RMSE values decreased by 56.03%-83.13% and 40.74%-72.20% (Table S3).
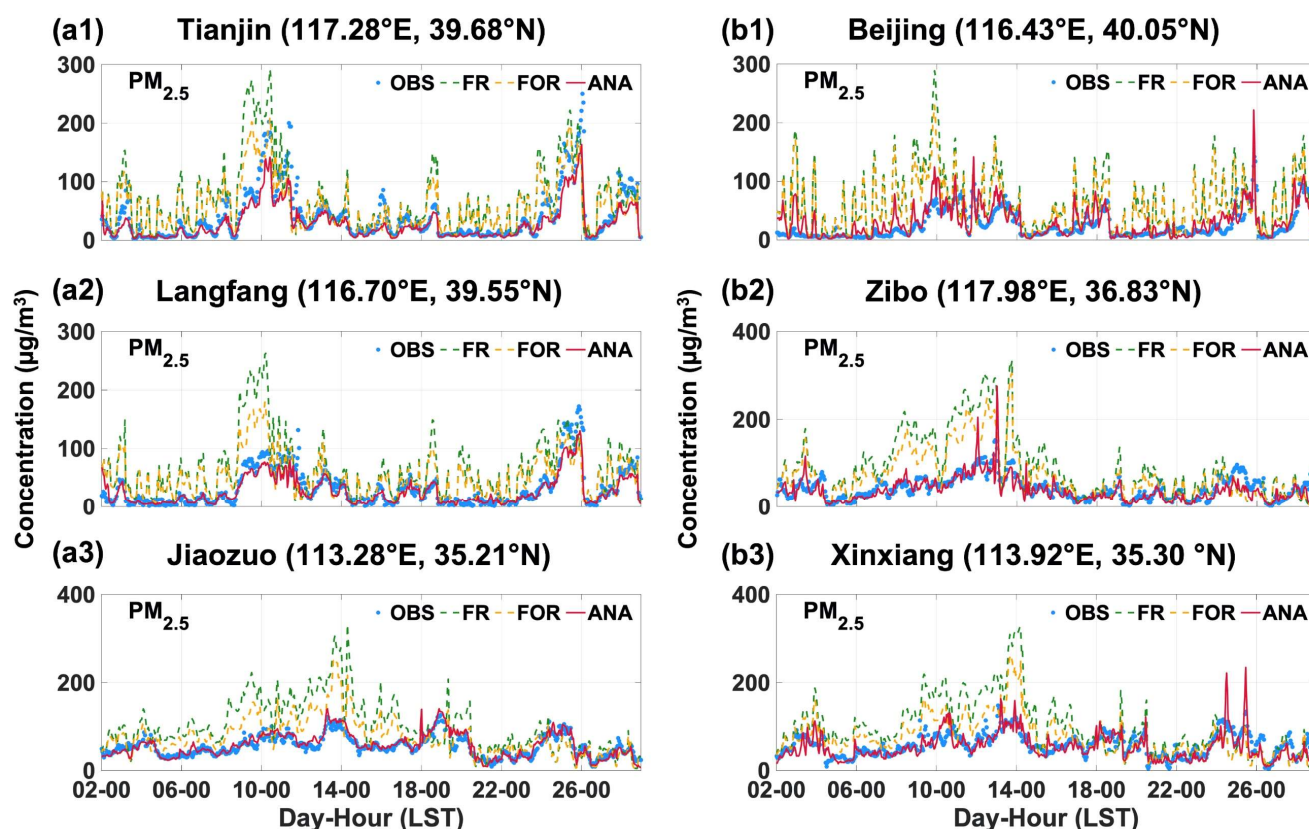
523
524 **Figure 9: Hourly variation of PM$_{2.5}$ in three representative DA sites (a1-a3) and three representative VE sites (b1-b3).**

525 **3.2.3 Assessment of spatial distribution in chemical components**

526 DA can improve the interpretation of model states in the analysis domain by using a limited number of observations. The

527 ability to represent spatial distribution accurately is a crucial performance for aerosol DA. Figure 10 displays the spatial

528 distribution of the monthly average mass concentrations for the five chemical components, including OBS, FR, FOR, ANA,

529 and analysis increment (INC). The spatial distributions of bias and statistical indicators for FR, FOR, and ANA are shown in

530 Fig. 11 and Fig. 12, respectively.

531
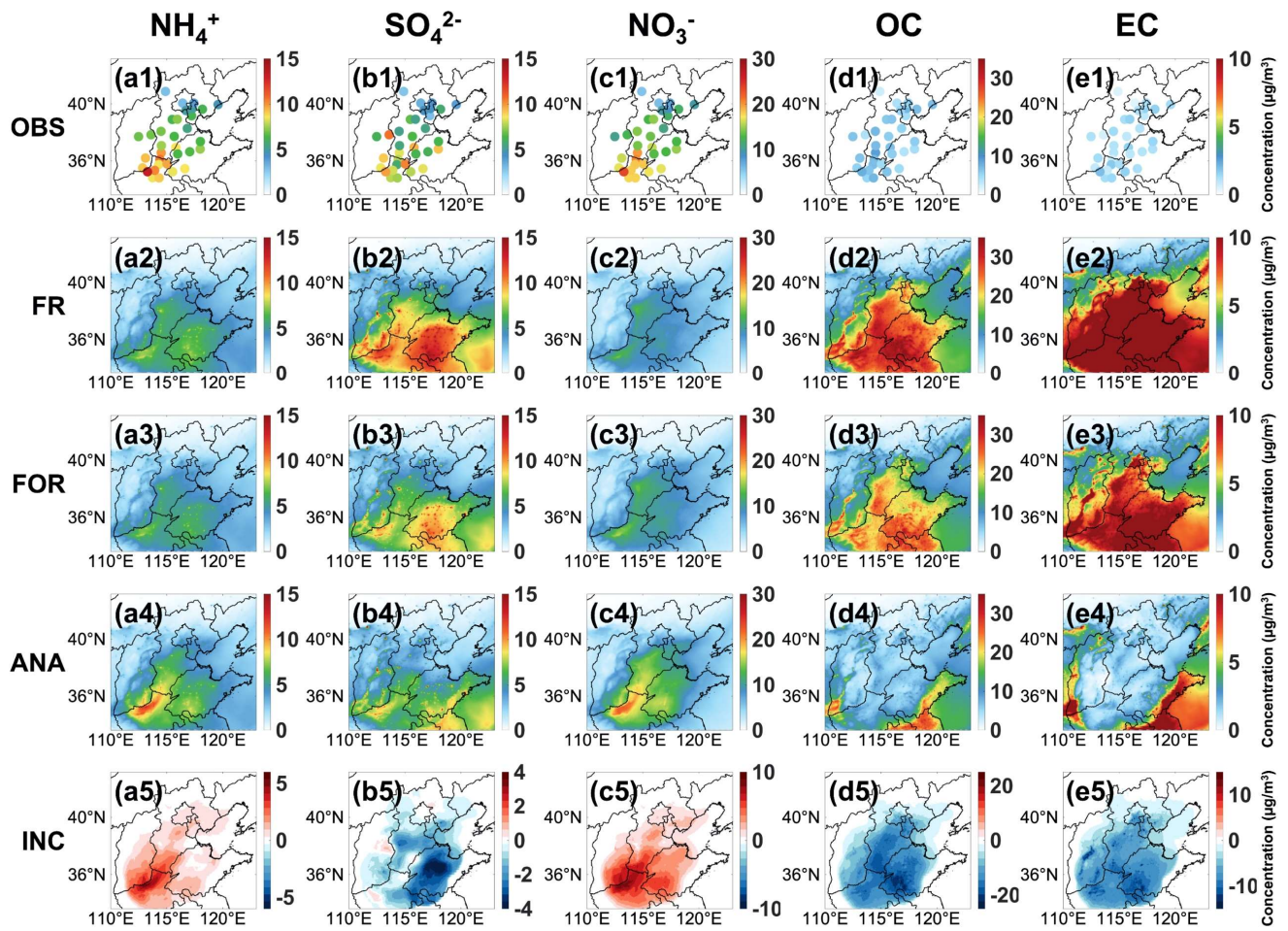
532 **Figure 10: Spatial concentration distribution of site observation (OBS, a1-e1), free-run field (FR, a2-e2), forecast field (FOR, a3-e3),**

533 **analysis field (ANA, a4-e4), and increment (INC) between ANA and FR (a5-e5) for five PM2.5 chemical components.**

534
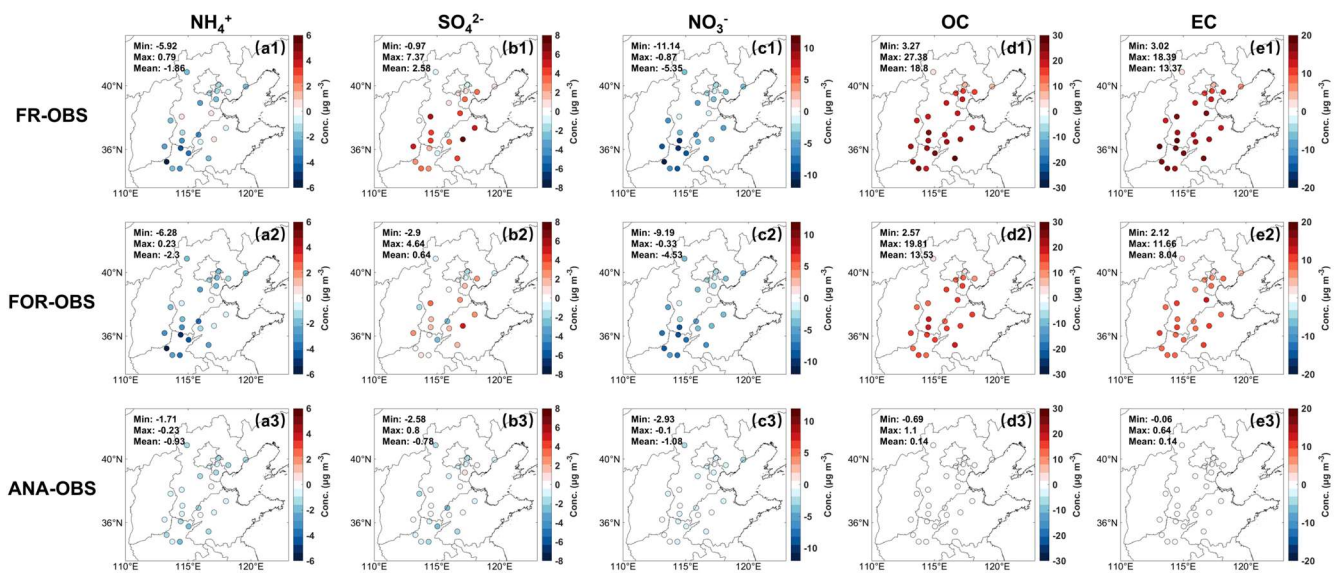
535 **Figure 11: Spatial distribution of DA-site bias for five PM2.5 chemical components from observation (OBS) for the free-running field**

536 **(FR, a1-e1), forecast field (FOR, a2-e2) and analysis field (ANA, a3-e3).**
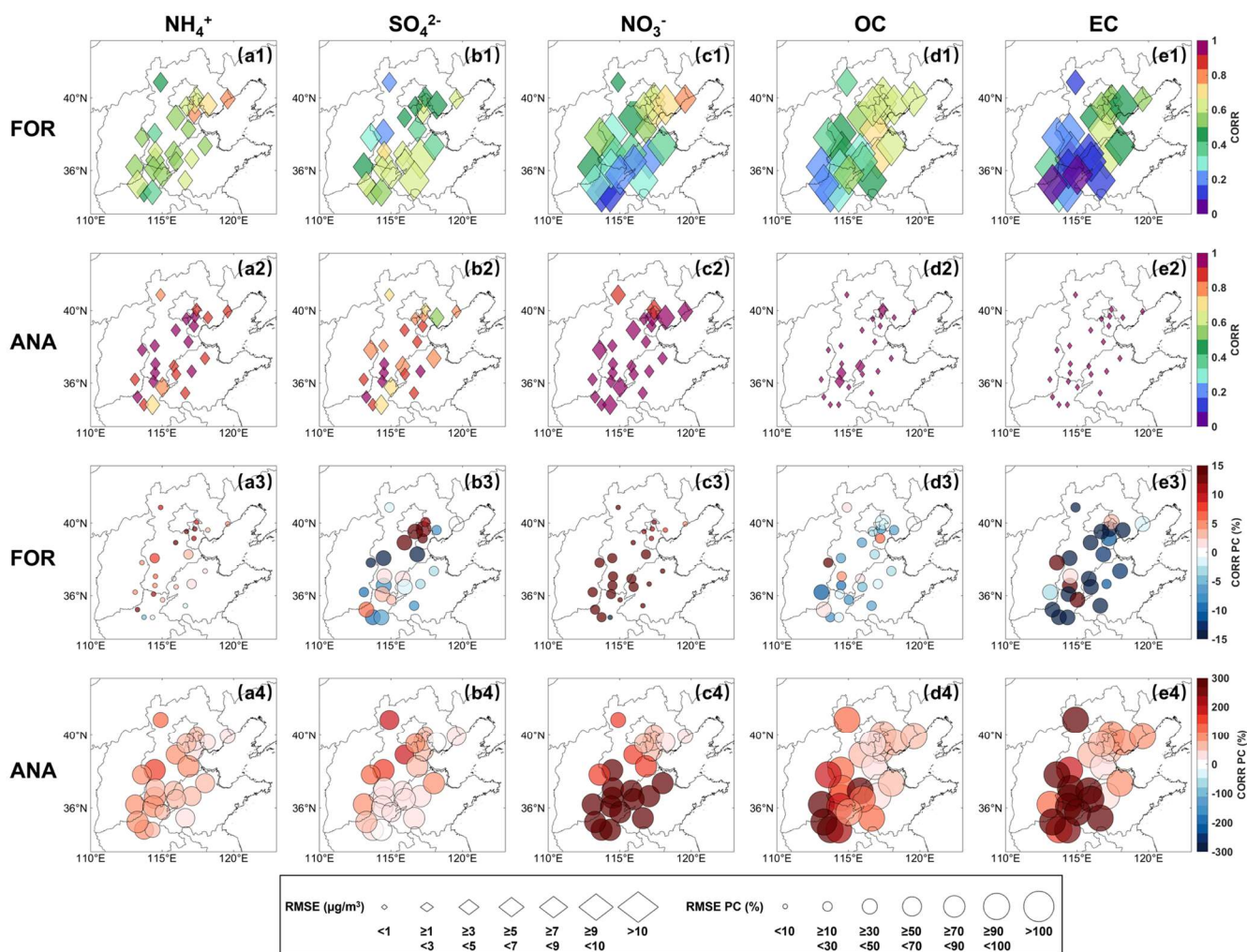
537

538 **Figure 12: Spatial distribution of DA-site statistical indicators for five PM$_{2.5}$ chemical components. (a1-e1) represents the values of**
539 **RMSE and CORR for the forecast field (FOR), (a2-e2) same as (a1-e1) but for analysis field (ANA), (a3-e3) represents the**
540 **improvement of RMSE and CORR for the forecast field (FOR), (a4-e4) same as (a3-e3) but for analysis field (ANA). The size**
541 **represents the value of RMSE in (a1-e2) and the improvement percentage compared to non-assimilation in (a3-e4), respectively.**

542   The spatial characteristics of NH$_4^+$ and NO$_3^-$ are similar. Compared to the OBS (Fig. 10a1 and c1), the FR (Fig. 10a2 and c2)

543   and FOR (Fig. 10a3 and c3) have failed to capture the high-value mass concentrations in the border area between Hebei

544   province, Shanxi province, Henan province, and Shandong province, especially in the northern region of Henan province. The

545   primary reason is the uncertainties in emission inventories in winter heating periods, which results in insufficient emission

546   statistics of gaseous precursors NOx and NH$_3$ (Aleksankina et al., 2018). After DA, this situation is significantly improved

547   with the ANA (Fig. 10a4 and c4). The INCs in the Beijing-Tianjin-Hebei region, Shanxi province, Henan province, and

548   Shandong province are positive (Fig. 10a5 and c5), indicating varying degrees of improvement in correcting the

549   underestimation of mass concentrations. Specifically, for NH$_4^+$ and NO$_3^-$ at DA sites, the biases between the OBS and ANA

550   are significantly reduced compared to the biases between the OBS and FR (Fig. 11), with the mean absolute bias decreasing

551   by 0.93 µg/m^3 and 4.27 µg/m^3, respectively. Moreover, the overall biases at VE sites also decrease (Fig. S5). As for the spatial

552   statistical indicators of NH$_4^+$ (Fig. 12a1 and a2), the CORR values in FOR and ANA range from 0.39 to 0.79 and 0.70 to 0.97,

553   respectively, and the RMSE values range from 3.16 µg/m^3 to 7.65 µg/m^3 and 1.20 µg/m^3 to 3.49 µg/m^3, respectively. As for

554 the spatial statistical indicators of NO_3^- (Fig. 12c1 and c2), the CORR values in FOR and ANA range from 0.09 to 0.76 and

555 0.89 to 0.99, respectively, and the RMSE values range from 4.88 µg/m^3 to 15.69 µg/m^3 and 1.34 µg/m^3 to 5.39 µg/m^3,

556 respectively. For the FOR, the improvement in accuracy for NO_3^- is more significant than that for NH_4^+, with the CORR values

557 of most DA sites increasing by more than 10% and the RMSE of most DA sites decreasing by not less than 10% (Fig. 12a3

558 and c3). For the ANA, NH_4^+ and NO_3^- exhibit significant improvements in CORR and RMSE, as most DA sites show over

559 150% in CORR and over 50% in RMSE (Fig. 12a4 and c4). Improvements can also be found in NH_4^+ and NO_3^- at VE sites

560 (Fig. S6). The spatial consistency of NH_4^+ and NO_3^- indicates that NH_4NO_3 is the primary aerosol chemical component,

561 highlighting the necessity of coordinated control of precursor NOx and NH_3.

562

563 Unlike NH_4^+ and NO_3^-, compared to the OBS (Fig. 10b1), the mass concentrations of SO_4^{2-} in the FR and FOR (Fig. 10b2 and

564 b3) are significantly overestimated, especially in Shandong province. In contrast, the ANA has dramatically improved (Fig.

565 10b4), with most areas showing negative INCs (Fig. 10b5). The mean absolute biases in DA and VE sites have decreased by

566 1.80 µg/m^3 and 2.68 µg/m^3, respectively (Fig. 11 and Fig. S5). Specifically, after DA, the CORR values of the FOR and ANA

567 range from 0.22 to 0.71 and 0.58-0.97, and the RMSE values range from 3.42 µg/m^3 to 11.07 µg/m^3 and 1.20 µg/m^3 to 4.30

568 µg/m^3, respectively (Fig. 12b1 and b2). The CORR and RMSE values in FOR have significantly improved (Fig. 12b3) at DA

569 sites around Beijing. While the CORR values in ANA have increased by more than 13%, with most DA sites showing an

570 increase of over 50%, and RMSE values have decreased by no less than 30%, with most DA sites showing a decrease of over

571 70% (Fig. 12b4). Besides, half of the VE sites show significant improvement in the CORR and RMSE in the FOR and ANA,

572 mainly due to their proximity to more DA sites (Fig. S6). The OBS and ANA indicate a considerable control in SO_4^{2-} pollution

573 during the winter heating period due to the emission reduction of gaseous precursors (Zhai et al., 2019; Yan et al., 2021).

574

575 The spatial distributions of OC and EC exhibit similarities (Fig. 10d1 and e1), consistent with the finding of a strong correlation

576 between OC and EC in winter (Cao et al., 2007). Since the low temperature and weakened photochemical reactions in winter

577 reduced secondary OC (SOC) generation, and primary OC (POC) and EC mainly originate from direct anthropogenic

578 emissions, such as combustion (Guo, 2016). Compared to the OBS, the mass concentrations in FR (Fig. 10d2-d3) and FOR

579 (Fig. 10e2-e3) are significantly overestimated over a wide range. Similar overestimations have also been reported in the global

580 reanalysis datasets of CAMS and MERRA-2, likely attributed to the hygroscopic growth scheme of carbonaceous aerosols in

581 the models, poorly constrained semi-volatile species escaping from primary organic aerosols (Soni et al., 2021), and aging

582 mechanisms in the models (Huang et al., 2013). After DA, the spatial distribution of the ANA aligns entirely with that of the

583 OBS (Fig. 10d4 and e4), with the improvements in all overestimations (Fig. 10d5 and e5) and the average biases of OC and

584 EC at DA sites both significantly decreasing to 0.14 µg/m³ (Fig. 11d3 and e3). The VE sites show similar results to the DA

585 sites, with average biases of less than 2 µg/m³ (Fig. S5d3 and e3). Specifically, for OC (Fig. 12d1 and d2), the CORR values

586 in FOR and ANA are 0.18-0.71 and 0.92-1.00, respectively, with RMSE values of 7.91 μg/m³-26.27 μg/m³ and 0.16 μg/m³-

587 1.45 μg/m³, respectively. For EC (Fig. 12e1 and e2), the CORR values in FOR and ANA are 0.01-0.66 and 0.97-1.00,

588 respectively, with RMSE values of 5.33 μg/m³-16.91 μg/m³ and 0.01 μg/m³-0.26 μg/m³, respectively. Although significant

589 improvements are not observed in FOR at some specific DA sites, the RMSE values at all DA sites decrease by 10%-50% (Fig.

590 12d3 and e3). The CORR values of OC and EC in ANA increase by more than 30%, with most DA sites exceeding 200%, and

591 the RMSE values decrease by more than 90% (Fig. 12d4 and e4). At VE sites (Fig. S6), significant improvements in the CORR

592 are not observed, but the RMSE values in the FOR and ANA decrease, which indicates that DA has limited benefits for whole

593 areas but can effectively reduce biases of entire regions.

594 **3.3 Compared to NAQPMS-PDAF v1.0 and global reanalysis dataset**

595 To comprehensively evaluate the competitiveness and superiority of NAQPMS-PDAF v2.0 in generating the reanalysis

596 datasets of the $PM_{2.5}$ chemical compositions, we assimilated the mass concentrations of the five $PM_{2.5}$ chemical components

597 from all sites (sum of DA sites and VE sites) in February 2022 to generate a reanalysis dataset. We compared our reanalysis

598 dataset with the global reanalysis (RA) datasets (CAMSRA and MERRA-2) and NAQPMS-PDAF v1.0 output. Figure 13

599 illustrates the spatial distribution of the monthly average mass concentrations for the five chemical components. Compared to

600 the OBS (Fig. 13a1 and c1), CAMSRA underestimates the NH_4^+ and NO_3^- concentrations and fails to capture the high-value

601 concentration in northern Henan Province (Fig. 13a2 and c2). Meanwhile, MERRA-2 overestimates the concentrations of

602 SO_4^{2-}, OC, and EC (Fig. 13b2, d2, and e2), particularly SO_4^{2-}, exhibiting a large region with inaccurately high concentrations.

603 Besides, CAMSRA (approximately 80*80 km²) and MERRA-2 (55*70 km²) have significantly lower spatial resolutions

604 compared to NAQPMS-PDAF v2.0 (5*5 km²). Therefore, NAQPMS-PDAF v2.0 provides a more detailed description of the

605 pollution characteristics of chemical components in Northern China and surrounding areas compared to RA.
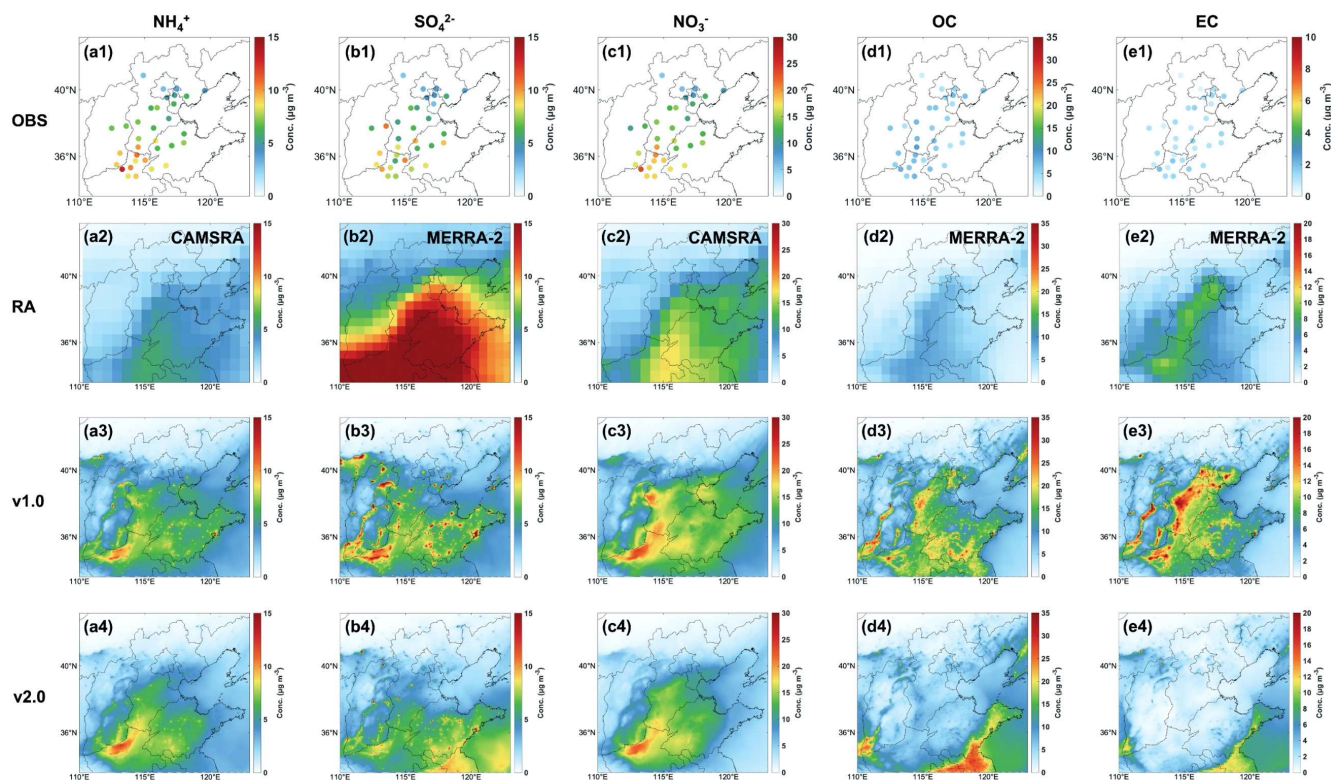
Figure 13: Spatial distribution of the monthly averaged concentration of five PM$_{2.5}$ chemical components for observations (OBS, a1-e1), global reanalysis data (RA, a2-e2), NAQPMS-PDAF v1.0 analysis data (a3-e3) and NAQPMS-PDAF v2.0 analysis data (a4-e4).

Although NAQPMS-PDAF v1.0 demonstrates a superior spatial representation of the five chemical components when compared to RA, it fails to capture the high-value concentrations of NH$_4^+$ in the northwest of Henan Province and correct the high-value concentrations of NH$_4^+$ in the central and western areas of Hebei Province (Fig. 13a3). Moreover, the scattered high-value concentrations of SO$_4^{2-}$ in the North China Plain do not align with the spatial characteristics of the OBS (Fig. 13b3). Notably, NAQPMS-PDAF v1.0 exhibits poor performance in interpreting OC and EC with significant overestimations in a wide range (Fig. 13d3 and e3), which indicates that NAQPMS-PDAF v1.0 is weaker than NAQPMS-PDAF v2.0 in terms of DA performance on chemical components, primarily due to insufficient propagation of observations. In NAQPMS-PDAF v2.0, the LKNETF algorithm with an adaptive forgetting factor is more suitable for the nonlinear and non-Gaussian situations compared to EnKFs in NAQPMS-PDAF v1.0, and the ensemble perturbation with non-Gaussian distribution can better represent the reasonable error distribution of model states.

Table 3 presents a quantitative comparison of three reanalysis datasets. Compared to the CORR of NAQPMS-PDAF v2.0 (0.86-0.99), the CORR of RA for the five chemical components is significantly lower (0.42-0.55). Moreover, NAQPMS-PDAF v1.0 exhibits significantly poorer consistency in SO$_4^{2-}$, OC, and EC, with CORR values ranging from 0.35 to 0.57. NAQPMS-PDAF v2.0 has lower overall RMSE values (0.14 μg/m^3-3.18 μg/m^3) compared to RA and NAQPMS-PDAF v1.0, with RMSE values ranging from 4.51 μg/m^3 to 12.27 μg/m^3 and 2.46 μg/m^3 to 15.50 μg/m^3, respectively. The characteristics of R^2 are similar to those of CORR and RMSE. For NH$_4^+$ and NO$_3^-$, NAQPMS-PDAF v2.0 (0.85 and 0.93) and v1.0 (0.80 and 0.96) are

626 much higher than RA (0.09 and 0.13). Notably, for SO$_4^{2-}$, OC, and EC, NAQPMS-PDAF v2.0 (0.74-0.98) is significantly

627 higher than v1.0 (-0.16-0.25) and RA (-0.15-0.25). Overall, NAQPMS-PDAF v2.0 more accurately and consistently interprets

628 the five chemical components, particularly for NH$_4^+$, SO$_4^{2-}$, OC, and EC. The reasons are summarized as follows. (1) The DA

629 frequency of CAMSRA is 12 hours, which is lower than the hourly DA frequency in NAQPMS-PDAF v2.0. (2) CAMSRA

630 only assimilates satellite retrievals (Inness et al., 2019), and MERRA-2 only assimilates aerosol optical depth (AOD) from

631 both ground-based and space-based remote sensing platforms (Randles et al., 2017). The aerosol optical information analysis

632 increment cannot be allocated to each chemical component accurately and reasonably due to the lack of a deterministic

633 relationship between aerosol optical information and PM$_{2.5}$ chemical components. (3) NAQPMS-PDAF v1.0 has evident DA

634 shortcomings for chemical components due to the limited DA algorithm under the assumption of a linear model or system,

635 inappropriate ensemble perturbation under the assumption of Gaussian distribution and inadequate observational modules. (4)

636 The state variable structure in NAQPMS-PDAF v1.0 cannot effectively mitigate the impact of spurious correlations between

637 chemical component variables, even when using analytical localization.

638 **Table 3: Statistical indicators (CORR, RMSE, R^2) of five PM$_{2.5}$ chemical components for global reanalysis data (RA), NAQPMS-**
639 **PDAF v1.0 analysis data and NAQPMS-PDAF v2.0 analysis data.**

Components	CORR			RMSE (µg/m^3)			R^2		
	RA	v1.0	v2.0	RA	v1.0	v2.0	RA	v1.0	v2.0
NH$_4^+$	0.49	0.90	0.92	5.59	2.53	2.22	0.09	0.80	0.85
SO$_4^{2-}$	0.55	0.57	0.86	12.27	5.45	2.61	0.25	0.25	0.74
NO$_3^-$	0.54	0.98	0.96	10.27	2.46	3.18	0.13	0.96	0.93
OC	0.50	0.42	0.97	4.51	12.92	0.93	0.15	-0.09	0.93
EC	0.42	0.35	0.99	7.59	15.50	0.14	-0.15	-0.16	0.98

640 **3.4 The uncertainty in NAQPMS-PDAF v2.0**

641 In ensemble DA, the ensemble members represent possible values of the model states, and the ensemble sampling can

642 determine the uncertainties of the model states. Therefore, the ensemble generation directly affects the propagation of

643 observations and subsequently impacts the final DA performance. Previous studies generated ensemble members based on the

644 uncertainties of emission species and the Gaussian-distribution assumption to satisfy the requirements of EnKFs algorithms

645 (Kong et al., 2021; Wang et al., 2022). However, the true error probability distribution of emission species is not an ideal

646 Gaussian distribution, and the assumption will introduce errors. In this study, we coupled the hybrid nonlinear DA algorithm

647 (LKNETF) with NAQPMS to handle the nonlinear and non-Gaussian situations, which combines the stability of LETKF with

648 the nonlinearity of LNETF. Therefore, we evaluate the performance of ensemble members with different uncertainties and

649 error probability distributions in NAQPMS-PDAF v2.0 through two groups of sensitivity experiments.

650

651 The first group of experiments (T1-T5) involves controlling the SO$_2$ uncertainty as a fixed value of 200% and transforming

652   the distribution of the perturbation coefficient matrix. The second group of experiments (M1-M5) focuses on assessing the

653   influence of SO_2 uncertainty on NH_4^+ and SO_4^{2-} DA based on a fixed non-Gaussian distribution (m3=1, m4=6). Figure 14

654   shows the statistical indicators of the five chemical components under different error probability distributions, including a

655   Gaussian distribution (T1) and four non-Gaussian distributions (T2-T5). The mean CRPS and RMSE in T2 and T4 are lower

656   than those in T1, T3, and T5, and the CORR values in T2 and T4 are higher than those in T1, T3, and T5, indicating that the

657   DA performance of non-Gaussian-distribution assumption is superior to that of Gaussian-distribution assumption. Moreover,

658   positively skewed non-Gaussian distribution performs better than negatively skewed distribution. Except for SO_4^{2-}, the

659   performance in T2 outweighs that in T4 for other chemical components, implying that higher kurtosis harms the chemical

660   components DA.
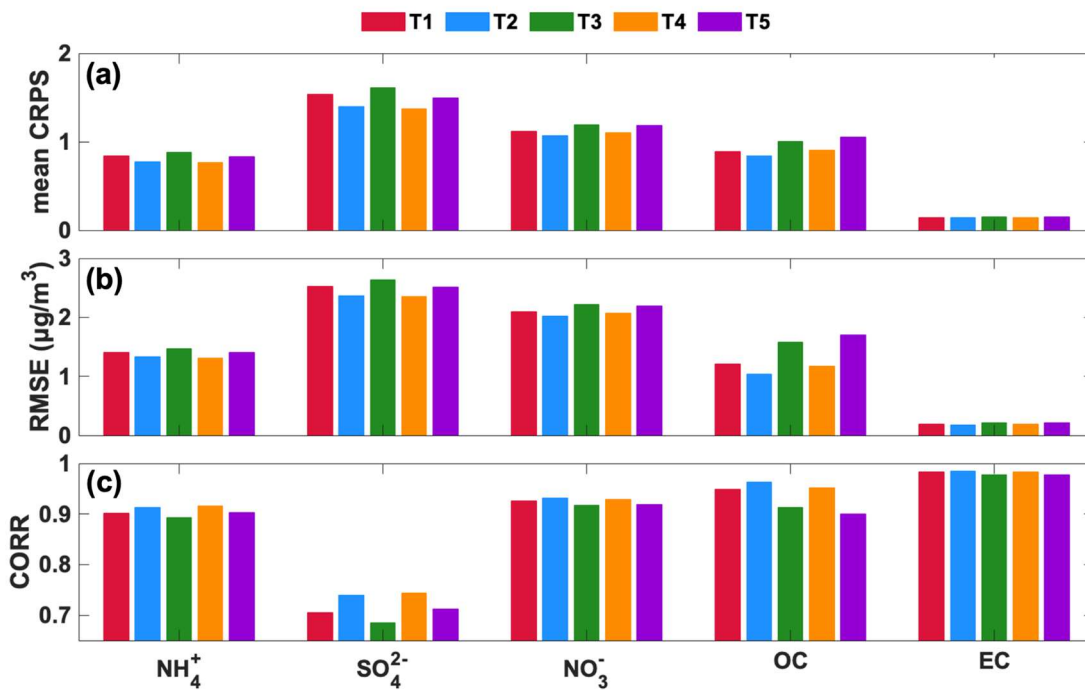
661

662   **Figure 14: Statistical indicators (mean CRPS (a), RMSE (b), and CORR (c)) of five PM$_{2.5}$ chemical components for five perturb**

663   **experiments based on distribution.**

664   SO_2 is a crucial precursor of NH_4^+ and SO_4^{2-}, and perturbing SO_2 affects the forecast and simulation of NH_4^+ and SO_4^{2-}. Table

665   4 presents statistical indicators of NH_4^+ and SO_4^{2-} analysis fields based on ensemble perturbations with different SO_2

666   uncertainties (12%-300%). Increasing the uncertainty of SO_2 from 12% to 200% leads to a decrease in the mean CRPS in the

667   SO_4^{2-} analysis field from 2.67 to 1.40, an increase in the CORR from 0.51 to 0.74, and a reduction in the RMSE from 4.10

668    $\mu g/m^3$ to 2.37 $\mu g/m^3$. Similarly, the mean CRPS in the NH_4^+ analysis field decreases from 0.98 to 0.77, the CORR increases

669   from 0.88 to 0.91, and the RMSE decreases from 1.55 $\mu g/m^3$ to 1.33 $\mu g/m^3$. It indicates that increasing the uncertainty of SO_2

670   improves the DA performance on NH_4^+ and SO_4^{2-} because the higher SO_2 uncertainty makes SO_2 perturbed sufficiently, and

671   the estimated error probability distribution is closer to the real distribution, resulting in a sufficient spread of observations.

672   However, when the uncertainty of SO_2 reaches 300%, the statistical indicators do not significantly improve and even worsen

673 because excessively high SO$_2$ uncertainty causes the estimated error probability distribution to deviate from the true

674 distribution. Thus, selecting appropriate uncertainties for emission species is crucial in aerosol chemical component DA.

675

676 To summarize, the non-Gaussian distribution assumption outperforms the Gaussian distribution assumption in NAQPMS-

677 PDAF v2.0. Positive skewness performs better than negative skewness, and excessively high kurtosis should be avoided.

678 Additionally, appropriately increasing the uncertainty of SO$_2$ enhances the DA performance of NH$_4^+$ and SO$_4^{2-}$. Future studies

679 should conduct more sensitivity experiments on emission species perturbation to determine the suitable schemes for different

680 aerosol chemical components.

681 **Table 4: Statistical indicators (mean CRPS (a), RMSE (b), and CORR (c)) of five PM$_{2.5}$ chemical components for five perturb**
682 **experiments based on SO$_2$ emission uncertainty.**

Experiment	SO$_4^{2-}$			NH$_4^+$		
	CRPS	CORR	RMSE	CRPS	CORR	RMSE
M1	2.67	0.51	4.10	0.98	0.88	1.55
M2	2.07	0.59	3.24	0.92	0.89	1.48
M3	1.61	0.69	2.63	0.83	0.91	1.39
M4	1.40	0.74	2.37	0.77	0.91	1.33
M5	1.41	0.74	2.39	0.78	0.91	1.33

683 **4 Conclusions**

684 In this paper, we online coupled NAQPMS with PDAF-OMI to develop a novel hybrid nonlinear DA system (NAQPMS-

685 PDAF v2.0) with level-2 parallelization based on a hybrid Kalman-Nonlinear Ensemble Transform Filter (LKNETF) for the

686 first time. Compared to NAQPMS-PDAF v1.0, NAQPMS-PDAF v2.0 with OMI can be applied with multiple component

687 types and nonlinear/non-Gaussian situations in chemical analysis to effectively interpret five PM$_{2.5}$ chemical components

688 (NH$_4^+$, SO$_4^{2-}$, NO$_3^-$, OC and EC), which is not achieved in previous studies. The background error covariance was calculated

689 by ensemble perturbation based on adaptive uncertainties and non-Gaussian distribution assumption of emission species. The

690 DA experiments were conducted based on 33 observational sites in Northern China and surrounding areas.

691

692 NAQPMS-PDAF v2.0 with LKNETF can maintain high accuracy and reliability in ensemble DA with an ensemble size of 10,

693 smaller than the traditional minimum of 20 ensemble members, as observed in prior ensemble assimilation studies. The FR

694 (free-run fields without DA) have a poor consistency with the observations, with the CORR values ranging from 0.32-0.56

695 and the R^2 values less than 0.3, showing that SO$_4^{2-}$, OC and EC are significantly overestimated, while NH$_4^+$ and NO$_3^-$ are

696 underestimated. A significant improvement was observed in the ANA (analysis fields) at the DA sites. The CORR values are

697 not less than 0.86, the RMSE and MAE values do not exceed 3.23 µg/m^3 and 1.49 µg/m^3, respectively, and R^2 is not less than

698 0.74. Specifically, the CORR values for NO$_3^-$, OC, and EC are not less than 0.96, and R^2 is not less than 0.93. The error

distributions of the five chemical components concentrate to 0 with the mean bias ranging from 0 ± 0.08 µg/m^3 to 1.02 ± 3.07 µg/m^3. These improvements are also found in the ANA at VE sites, indicating an excellent DA performance of NAQPMS-PDAF v2.0.

The ability of NAQPMS-PDAF v2.0 to interpret the spatiotemporal characteristics of the five chemical components was examined. For temporal variations, compared to the FR and FOR (forecast fields), the ANA closely aligned with the OBS (observations) and accurately captured the peak concentrations of SO_4^{2-}, NO_3^-, and NH_4^+ on specific periods (such as February 25th), indicating good consistency and accurate characterization. Specifically, the CORR of the ANA at the six representative sites increased by 13.64%-89.58% and 17.19%-75.00%, respectively, while the RMSE decreased by 56.03%-83.13% and 40.74%-72.20%. For spatial distributions, after DA, both NH_4^+ and NO_3^- with positive analysis increments exhibit significant improvements in CORR and RMSE, as most DA sites show improvements of over 150% in CORR and over 50% in RMSE. SO_4^{2-}, OC, and EC with negative analysis increments were also improved. Especially for OC and EC, the improvements of CORR and RMSE at most DA sites were over 200% and over 90%, respectively. The improvements at VE sites were also identified. Consequently, DA successfully aligned the spatiotemporal characteristics of the ANA with OBS and significantly reduced the biases of five chemical components.

Compared to the global reanalysis datasets (CORR: 0.42-0.55, RMSE: 4.51-12.27 µg/m^3) and NAQPMS-PDAF v1.0 (CORR: 0.35-0.98, RMSE: 2.46-15.50 µg/m^3), the NAQPMS-PDAF v2.0 (CORR: 0.86-0.99, RMSE: 0.14-3.18 µg/m^3) has significant superiority in generating the reanalysis datasets of the PM$_{2.5}$ chemical compositions with high spatiotemporal resolution. Besides, NAQPMS-PDAF v1.0 cannot capture the high-value concentrations and exhibits poor performance when interpreting SO_4^{2-}, OC, and EC with CORR values ranging from 0.35 to 0.57. In contrast, NAQPMS-PDAF v2.0 interprets the five chemical components more accurately and consistently.

Finally, the uncertainties of NAQPMS-PDAF v2.0 are examined by identifying the influence of ensemble generation on ensemble DA performance. The non-Gaussian distribution assumption outperforms the Gaussian distribution assumption in NAQPMS-PDAF v2.0. Positive skewness performs better than negative skewness, and excessively high kurtosis should be avoided. Additionally, appropriately increasing the uncertainty of SO$_2$ enhances the DA performance of NH$_4^+$ and SO$_4^{2-}$. Future studies should conduct more sensitivity experiments on emission species perturbation to determine the suitable schemes for different aerosol chemical components.

The novel hybrid nonlinear DA system (NAQPMS-PDAF v2.0) can be effectively applied in the interpretation of chemical components and outperform in generating the reanalysis dataset of the five PM$_{2.5}$ chemical components with high accuracy

731 and high consistency, thus providing the sufficient channel to investigate the spatiotemporal characteristics, identify the

732 regional transport and prevent and control aerosol composition pollution. In future work, we plan to research the vertical DA

733 of chemical components, introduce more vertical information from more observational platforms, and verify the simultaneous

734 DA performance of surface and vertical mass concentrations.

735

Code and data availability

737 The source codes and related data in our work are openly accessible at https://doi.org/10.5281/zenodo.10886914 (Li et al.,
738 2024).

Author contributions

740 HL developed the data assimilation system, performed numerical experiments, carried out the analysis, and wrote the original
741 manuscript. TY provided scientific guidance, designed the paper structure, and wrote this paper. LN developed PDAF and
742 provided help for the model code. DWZ, DZ, and GT provided $PM_{2.5}$ chemical component data. HW provided help with the
743 model code. YS, PF, HS, and ZW did overall supervision. All authors reviewed and revised this paper.

Competing interests

745 The contact author has declared that neither they nor their co-authors have any competing interests.

Acknowledgements

747 This work was supported by the National Key Research and Development Program for Young Scientists of China (No.
748 2022YFC3704000), the National Natural Science Foundation of China (No. 42275122), and the National Key Scientific and
749 Technological Infrastructure project "Earth System Science Numerical Simulator Facility" (EarthLab). Ting Yang would like
750 to express gratitude towards the Program of the Youth Innovation Promotion Association (CAS). We thank the Big Data Cloud
751 Service Infrastructure Platform (BDCSIP) for providing computing resources.

752

Reference

Aleksankina, K., Heal, M. R., Dore, A. J., Van Oijen, M., and Reis, S.: Global sensitivity and uncertainty analysis of an atmospheric chemistry transport model: the FRAME model (version 9.15.0) as a case study, Geosci. Model Dev., 11, 1653-1664, https://doi.org/10.5194/gmd-11-1653-2018, 2018.

Ali, A., Amin, S. E., Ramadan, H. H., and Tolba, M. F.: Enhancement of OMI aerosol optical depth data assimilation using artificial neural network, Neural Computing and Applications, 23, 2267-2279, https://doi.org/10.1007/s00521-012-1178-9, 2013.

Alves, C., Evtyugina, M., Vicente, E., Vicente, A., Rienda, I. C., de la Campa, A. S., Tomé, M., and Duarte, I.: $PM_{2.5}$ chemical composition and health risks by inhalation near a chemical complex, J. Environ. Sci., 124, 860-874, https://doi.org/10.1016/j.jes.2022.02.013, 2023.

Amante, C. and Eakins, B. W.: ETOPO1 arc-minute global relief model: procedures, data sources and analysis, 2009.

Arthur, D. and Vassilvitskii, S.: K-means++: the advantages of careful seeding, Proceedings of the eighteenth annual ACM-SIAM symposium on Discrete algorithms, 1027-1035, https://dl.acm.org/doi/10.5555/1283383.1283494, 2007

Bao, Y., Zhu, L., Guan, Q., Guan, Y., Lu, Q., Petropoulos, G. P., Che, H., Ali, G., Dong, Y., Tang, Z., Gu, Y., Tang, W., and Hou, Y.: Assessing the impact of Chinese FY-3/MERSI AOD data assimilation on air quality forecasts: Sand dust events in northeast China, Atmos. Environ., 205, 78-89, https://doi.org/10.1016/j.atmosenv.2019.02.026, 2019.

Bell, M. L., Dominici, F., Ebisu, K., Zeger, S. L., and Samet, J. M.: Spatial and temporal variation in $PM_{2.5}$ chemical composition in the United States for health effects studies, Environ. Health Perspect., 115, 989-995, https://doi.org/10.1289/ehp.9621, 2007.

Bishop, C. H., Etherton, B. J., and Majumdar, S. J.: Adaptive Sampling with the Ensemble Transform Kalman Filter. Part I: Theoretical Aspects, Mon. Weather Rev., 129, 420-436, https://doi.org/10.1175/1520-0493(2001)129<0420:ASWTET>2.0.CO;2, 2001.

Cao, J. J., Lee, S. C., Chow, J. C., Watson, J. G., Ho, K. F., Zhang, R. J., Jin, Z. D., Shen, Z. X., Chen, G. C., Kang, Y. M., Zou, S. C., Zhang, L. Z., Qi, S. H., Dai, M. H., Cheng, Y., and Hu, K.: Spatial and seasonal distributions of carbonaceous aerosols over China, J. Geophys Res.-Atmos., 112, https://doi.org/10.1029/2006jd008205, 2007.

Chai, T., Kim, H. C., Pan, L., Lee, P., and Tong, D.: Impact of moderate resolution imaging spectroradiometer aerosol optical depth and airnow $PM_{2.5}$ assimilation on community multi-scale air quality aerosol predictions over the contiguous United States, J. Geophys Res., 122, 5399-5415, https://doi.org/10.1002/2016JD026295, 2017.

Chang, W., Zhang, Y., Li, Z., Chen, J., and Li, K.: Improving the sectional Model for Simulating Aerosol Interactions and Chemistry (MOSAIC) aerosols of the Weather Research and Forecasting-Chemistry (WRF-Chem) model with the revised Gridpoint Statistical Interpolation system and multi-wavelength aerosol optical measurements: The dust aerosol observation campaign at Kashi, near the Taklimakan Desert, northwestern China, Atmos. Chem. Phys., 21, 4403-4430, https://doi.org/10.5194/acp-21-4403-2021, 2021.

Chang, W., Liao, H., Xin, J., Li, Z., Li, D., and Zhang, X.: Uncertainties in anthropogenic aerosol concentrations and direct radiative forcing induced by emission inventories in eastern China, Atmos. Res., 166, 129-140, https://doi.org/10.1016/j.atmosres.2015.06.021, 2015.

Cheng, Y., Dai, T., Goto, D., A J Schutgens, N., Shi, G., and Nakajima, T.: Investigating the assimilation of CALIPSO global aerosol vertical observations using a four-dimensional ensemble Kalman filter, Atmos. Chem. Phys., 19, 13445-13467, https://doi.org/10.5194/acp-19-13445-2019, 2019.

Cheynet, E.: Non-Gaussian process generation, https://github.com/ECheynet/Gaussian_to_nonGaussian/releases/tag/v1.2, GitHub. Retrieved July 7, 2024.

Constantinescu, E. M., Sandu, A., Chai, T., and Carmichael, G. R.: Assessment of ensemble-based chemical data assimilation in an idealized setting, Atmos. Environ., 41, 18-36, https://doi.org/10.1016/j.atmosenv.2006.08.006, 2007.

Dai, T., Schutgens, N. A. J., Goto, D., Shi, G., and Nakajima, T.: Improvement of aerosol optical properties modeling over Eastern Asia with MODIS AOD assimilation in a global non-hydrostatic icosahedral aerosol transport model, Environ. Pollut., 195, 319-329, https://doi.org/10.1016/j.envpol.2014.06.021, 2014.

Du, W., Dada, L., Zhao, J., Chen, X., Daellenbach, K. R., Xie, C., Wang, W., He, Y., Cai, J., Yao, L., Zhang, Y., Wang, Q., Xu,

W., Wang, Y., Tang, G., Cheng, X., Kokkonen, T. V., Zhou, W., Yan, C., Chu, B., Zha, Q., Hakala, S., Kurppa, M., Järvi, L., Liu, Y., Li, Z., Ge, M., Fu, P., Nie, W., Bianchi, F., Petäjä, T., Paasonen, P., Wang, Z., Worsnop, D. R., Kerminen, V.-M., Kulmala, M., and Sun, Y.: A 3D study on the amplification of regional haze and particle growth by local emissions, npj Climate and Atmospheric Science, 4, 4, https://doi.org/10.1038/s41612-020-00156-5, 2021.

Evensen, G.: Sequential data assimilation with a nonlinear quasi-geostrophic model using Monte Carlo methods to forecast error statistics, J. Geophys Res., 99, https://doi.org/10.1029/94jc00572, 1994.

Evensen, G.: The Ensemble Kalman Filter: Theoretical formulation and practical implementation, Ocean Dynamics, 53, 343-367, https://doi.org/10.1007/s10236-003-0036-9, 2003.

Friedman, J. H., Bentley, J. L., and Finkel, R. A.: An algorithm for finding best matches in logarithmic expected time, ACM T. Math. Software, 3, 209-226, https://doi.org/10.1145/355744.355745, 1977.

Ge, B., Wang, Z., Xu, X., Wu, J., Yu, X., and Li, J.: Wet deposition of acidifying substances in different regions of China and the rest of East Asia: Modeling with updated NAQPMS, Environ. Pollut., 187, 10-21, https://doi.org/10.1016/j.envpol.2013.12.014, 2014.

Ge, X., He, Y., Sun, Y., Xu, J., Wang, J., Shen, Y., and Chen, M.: Characteristics and Formation Mechanisms of Fine Particulate Nitrate in Typical Urban Areas in China, Atmosphere, 8, https://doi.org/10.3390/atmos8030062, 2017.

Gordon, N. J., Salmond, D. J., and Smith, A. F.: Novel approach to nonlinear/non-Gaussian Bayesian state estimation, IEE Proc.-F, 140, 107-113, https://doi.org/10.1049/ip-f-2.1993.0015, 1993.

Guo, Y.: Characteristics of size-segregated carbonaceous aerosols in the Beijing-Tianjin-Hebei region, Environ. Sci. Pollut. R., 23, 13918-13930, https://doi.org/10.1007/s11356-016-6538-z, 2016.

Ha, S.: Implementation of aerosol data assimilation in WRFDA (v4.0.3) for WRF-Chem (v3.9.1) using the RACM/MADE-VBS scheme, Geosci. Model Dev., 15, 1769-1788, https://doi.org/10.5194/gmd-15-1769-2022, 2022.

Hamill, T. M. and Snyder, C.: A Hybrid Ensemble Kalman Filter–3D Variational Analysis Scheme, Mon. Weather Rev., 128, 2905-2919, https://doi.org/10.1175/1520-0493(2000)128<2905:AHEKFV>2.0.CO;2, 2000.

Hersbach, H.: Decomposition of the continuous ranked probability score for ensemble prediction systems, Wea. Forecasting, 15, 559-570, https://doi.org/10.1175/1520-0434(2000)015<0559:DOTCRP>2.0.CO;2, 2000.

Horowitz, L. W., Walters, S., Mauzerall, D. L., Emmons, L. K., Rasch, P. J., Granier, C., Tie, X., Lamarque, J. F., Schultz, M. G., Tyndall, G. S., Orlando, J. J., and Brasseur, G.P.: A global simulation of tropospheric ozone and related tracers: Description and evaluation of MOZART, version 2, J. Geophys Res.-Atmos., 108, https://doi.org/10.1029/2002JD002853, 2003.

Houtekamer, P. L. and Zhang, F.: Review of the Ensemble Kalman Filter for Atmospheric Data Assimilation, Mon. Weather Rev., 144, 4489-4532, https://doi.org/10.1175/mwr-d-15-0440.1, 2016.

Huang, B., Pagowski, M., Trahan, S., Martin, C. R., Tangborn, A., Kondragunta, S., and Kleist, D. T.: JEDI-Based Three-Dimensional Ensemble-Variational Data Assimilation System for Global Aerosol Forecasting at NCEP, J. Adv. Model. Earth Sy., 15, https://doi.org/10.1029/2022ms003232, 2023.

Huang, Y., Wu, S., Dubey, M. K., and French, N. H. F.: Impact of aging mechanism on model simulated carbonaceous aerosols, Atmos. Chem. Phys., 13, 6329-6343, https://doi.org/10.5194/acp-13-6329-2013, 2013.

Huneeus, N., Boucher, O., and Chevallier, F.: Atmospheric inversion of SO_2 and primary aerosol emissions for the year 2010, Atmos. Chem. Phys., 13, 6555-6573, https://doi.org/10.5194/acp-13-6555-2013, 2013.

Huneeus, N., Chevallier, F., and Boucher, O.: Estimating aerosol emissions by assimilating observed aerosol optical depth in a global aerosol model, Atmos. Chem. Phys., 12, 4585-4606, https://doi.org/10.5194/acp-12-4585-2012, 2012.

Hunt, B. R., Kostelich, E. J., and Szunyogh, I.: Efficient data assimilation for spatiotemporal chaos: A local ensemble transform Kalman filter, Physica D, 230, 112-126, https://doi.org/10.1016/j.physd.2006.11.008, 2007.

Inness, A., Ades, M., Agustí-Panareda, A., Barré, J., Benedictow, A., Blechschmidt, A. M., Dominguez, J. J., Engelen, R., Eskes, H., Flemming, J., Huijnen, V., Jones, L., Kipling, Z., Massart, S., Parrington, M., Peuch, V. H., Razinger, M., Remy, S., Schulz, M., and Suttie, M.: The CAMS reanalysis of atmospheric composition, Atmos. Chem. Phys., 19, 3515-3556, https://doi.org/10.5194/acp-19-3515-2019, 2019.

Jia, J., Cheng, S., Liu, L., Lang, J., Wang, G., Chen, G., and Liu, X.: An Integrated WRF-CAMx Modeling Approach for Impact Analysis of Implementing the Emergency $PM_{2.5}$ Control Measures during Red Alerts in Beijing in December 2015,

Aerosol Air Qual. Res., 17, 2491-2508, https://doi.org/10.4209/aaqr.2017.01.0009, 2017.

Jin, J., Segers, A., Heemink, A., Yoshida, M., Han, W., and Lin, H. X.: Dust Emission Inversion Using Himawari-8 AODs Over East Asia: An Extreme Dust Event in May 2017, J. Adv. Model. Earth Sy., 11, 446-467, https://doi.org/10.1029/2018MS001491, 2019.

Jolliffe, I. T. and Stephenson, D. B.: Forecast verification: a practitioner's guide in atmospheric science, John Wiley & Sons, https://doi.org/10.1002/9781119960003, 2012.

Khanna, I., Khare, M., Gargava, P., and Khan, A. A.: Effect of $PM_{2.5}$ chemical constituents on atmospheric visibility impairment, Journal of the Air & Waste Management Association, 68, 430-437, https://doi.org/10.1080/10962247.2018.1425772, 2018.

Kim, G., Lee, S., Im, J., Song, C.-K., Kim, J., and Lee, M.-i.: Aerosol data assimilation and forecast using Geostationary Ocean Color Imager aerosol optical depth and in-situ observations during the KORUS-AQ observing period, GISci. Remote Sens., 58, 1175-1194, https://doi.org/10.1080/15481603.2021.1972714, 2021.

Kong, L., Tang, X., Zhu, J., Wang, Z., Li, J., Wu, H., Wu, Q., Chen, H., Zhu, L., Wang, W., Liu, B., Wang, Q., Chen, D., Pan, Y., Song, T., Li, F., Zheng, H., Jia, G., Lu, M., Wu, L., and Carmichael, G. R.: A 6-year-long (2013–2018) high-resolution air quality reanalysis dataset in China based on the assimilation of surface observations from CNEMC, Earth Syst. Sci. Data, 13, 529-570, https://doi.org/10.5194/essd-13-529-2021, 2021.

Kumar, R., Ghude, S. D., Biswas, M., Jena, C., Alessandrini, S., Debnath, S., Kulkarni, S., Sperati, S., Soni, V. K., Nanjundiah, R. S., and Rajeevan, M.: Enhancing Accuracy of Air Quality and Temperature Forecasts During Paddy Crop Residue Burning Season in Delhi Via Chemical Data Assimilation, J. Geophys Res.-Atmos., 125, https://doi.org/10.1029/2020JD033019, 2020.

Kurtz, W., He, G., Kollet, S. J., Maxwell, R. M., Vereecken, H., and Hendricks Franssen, H. J.: TerrSysMP–PDAF (version 1.0): a modular high-performance data assimilation framework for an integrated land surface–subsurface model, Geosci. Model Dev., 9, 1341-1360, https://doi.org/10.5194/gmd-9-1341-2016, 2016.

Lawson, W. G. and Hansen, J. A.: Implications of Stochastic and Deterministic Filters as Ensemble-Based Data Assimilation Methods in Varying Regimes of Error Growth, Mon. Weather Rev., 132, 1966-1981, https://doi.org/10.1175/1520-0493(2004)132<1966:IOSADF>2.0.CO;2, 2004.

Li, H., Yang, T., Du, Y., Tan, Y., and Wang, Z.: Interpreting hourly mass concentrations of $PM_{2.5}$ chemical components with an optimal deep-learning model. J. Environ. Sci., 151, 125-139, https://doi.org/10.1016/j.jes.2024.03.037, 2025.

Li, H., Yang, T., and Wang, H.: NAQPMS-PDAF v2.0, Zenodo [code and data set], https://doi.org/10.5281/zenodo.10886914, 2024.

Li, J., Li, X., Carlson, B. E., Kahn, R. A., Lacis, A. A., Dubovik, O., and Nakajima, T.: Reducing multisensor satellite monthly mean aerosol optical depth uncertainty: 1. Objective assessment of current AERONET locations, J. Geophys Res.-Atmos., 121, 609-627, https://doi.org/10.1002/2016JD025469, 2016.

Li, J., Dong, Y., Song, Y., Dong, B., van Donkelaar, A., Martin, R. V., Shi, L., Ma, Y., Zou, Z., and Ma, J.: Long-term effects of $PM_{2.5}$ components on blood pressure and hypertension in Chinese children and adolescents, Environ. Int., 161, 107134, https://doi.org/10.1016/j.envint.2022.107134, 2022a.

Li, S., Chen, L., Huang, G., Lin, J., Yan, Y., Ni, R., Huo, Y., Wang, J., Liu, M., Weng, H., Wang, Y., and Wang, Z.: Retrieval of surface $PM_{2.5}$ mass concentrations over North China using visibility measurements and GEOS-Chem simulations, Atmos. Environ., 222, https://doi.org/10.1016/j.atmosenv.2019.117121, 2020.

Li, Y., Wang, X., Li, J., Zhu, L., and Chen, Y.: Numerical Simulation of Topography Impact on Transport and Source Apportionment on $PM_{2.5}$ in a Polluted City in Fenwei Plain, Atmosphere, 13, 233, https://doi.org/10.3390/atmos13020233, 2022b.

Lin, G. Y., Chen, H. W., Chen, B. J., and Chen, S. C.: A machine learning model for predicting $PM_{2.5}$ and nitrate concentrations based on long-term water-soluble inorganic salts datasets at a road site station, Chemosphere, 289, https://doi.org/10.1016/j.chemosphere.2021.133123, 2022.

Liu, Y., Liu, J., Li, C., Yu, F., and Wang, W.: Effect of the Assimilation Frequency of Radar Reflectivity on Rain Storm Prediction by Using WRF-3DVAR, Remote Sens., 13, https://doi.org/10.3390/rs13112103, 2021.

Lloyd, S.: Least squares quantization in PCM, IEEE T. Inform. Theory, 28, 129-137, https://doi.org/10.1109/TIT.1982.1056489, 1982.

Luo, X., Liu, X., Pan, Y., Wen, Z., Xu, W., Zhang, L., Kou, C., Lv, J., and Goulding, K.: Atmospheric reactive nitrogen concentration and deposition trends from 2011 to 2018 at an urban site in north China, Atmos. Environ., 224, https://doi.org/10.1016/j.atmosenv.2020.117298, 2020.

Lv, Z., Wei, W., Cheng, S., Han, X., and Wang, X.: Meteorological characteristics within boundary layer and its influence on $PM_{2.5}$ pollution in six cities of North China based on WRF-Chem, Atmos. Environ., 228, https://doi.org/10.1016/j.atmosenv.2020.117417, 2020.

Lynch, P., Reid, J. S., Westphal, D. L., Zhang, J., Hogan, T. F., Hyer, E. J., Curtis, C. A., Hegg, D. A., Shi, Y., Campbell, J. R., Rubin, J. I., Sessions, W. R., Turk, F. J., and Walker, A. L.: An 11-year global gridded aerosol optical thickness reanalysis (v1.0) for atmospheric and climate sciences, Geosci. Model Dev., 9, 1489-1522, https://doi.org/10.5194/gmd-9-1489-2016, 2016.

Mallet, V. and Sportisse, B.: Uncertainty in a chemistry-transport model due to physical parameterizations and numerical approximations: An ensemble approach applied to ozone modeling, J. Geophys Res.-Atmos., 111, https://doi.org/10.1029/2005jd006149, 2006.

Miao, R., Chen, Q., Zheng, Y., Cheng, X., Sun, Y., Palmer, P. I., Shrivastava, M., Guo, J., Zhang, Q., Liu, Y., Tan, Z., Ma, X., Chen, S., Zeng, L., Lu, K., and Zhang, Y.: Model bias in simulating major chemical components of $PM_{2.5}$ in China, Atmos. Chem. Phys., 20, 12265-12284, https://doi.org/10.5194/acp-20-12265-2020, 2020.

Ming, L., Jin, L., Li, J., Fu, P., Yang, W., Liu, D., Zhang, G., Wang, Z., and Li, X.: $PM_{2.5}$ in the Yangtze River Delta, China: Chemical compositions, seasonal variations, and regional pollution events, 223, 200-212, 2017.

Mingari, L., Folch, A., Prata, A. T., Pardini, F., Macedonio, G., and Costa, A.: Data assimilation of volcanic aerosol observations using FALL3D+PDAF, Atmos. Chem. Phys., 22, 1773-1792, https://doi.org/10.5194/acp-22-1773-2022, 2022.

Miyazaki, K., Eskes, H. J., Sudo, K., Takigawa, M., van Weele, M., and Boersma, K. F.: Simultaneous assimilation of satellite NO_2, O_3, CO, and HNO_3 data for the analysis of tropospheric chemical composition and emissions, Atmos. Chem. Phys., 12, 9545-9579, https://doi.org/10.5194/acp-12-9545-2012, 2012.

Nerger, L.: On Serial Observation Processing in Localized Ensemble Kalman Filters, Mon. Weather Rev., 143, 1554-1567, https://doi.org/10.1175/mwr-d-14-00182.1, 2015.

Nerger, L.: Data assimilation for nonlinear systems with a hybrid nonlinear Kalman ensemble transform filter, Q. J. Roy. Meteor. Soc., 148, 620-640, https://doi.org/10.1002/qj.4221, 2022.

Nerger, L., Tang, Q., and Mu, L.: Efficient ensemble data assimilation for coupled models with the Parallel Data Assimilation Framework: example of AWI-CM (AWI-CM-PDAF 1.0), Geosci. Model Dev., 13, 4305-4321, https://doi.org/10.5194/gmd-13-4305-2020, 2020.

Nerger, L., Janjić, T., Schröter, J., and Hiller, W.: A Unification of Ensemble Square Root Kalman Filters, Mon. Weather Rev., 140, 2335-2345, https://doi.org/10.1175/mwr-d-11-00102.1, 2012.

Nishizawa, T., Sugimoto, N., Matsui, I., Shimizu, A., and Okamoto, H.: Algorithms to retrieve optical properties of three component aerosols from two-wavelength backscatter and one-wavelength polarization lidar measurements considering nonsphericity of dust, J. Quant. Spectrosc. Ra., 112, 254-267, https://doi.org/10.1016/j.jqsrt.2010.06.002, 2011.

Nishizawa, T., Okamoto, H., Takemura, T., Sugimoto, N., Matsui, I., and Shimizu, A.: Aerosol retrieval from two-wavelength backscatter and one-wavelength polarization lidar measurement taken during the MR01K02 cruise of the R/V Mirai and evaluation of a global aerosol transport model, J. Geophys. Res.-Atmos., 113, https://doi.org/10.1029/2007jd009640, 2008.

Nishizawa, T., Sugimoto, N., Matsui, I., Shimizu, A., Hara, Y., Itsushi, U., Yasunaga, K., Kudo, R., and Kim, S. W.: Ground-based network observation using Mie-Raman lidars and multi-wavelength Raman lidars and algorithm to retrieve distributions of aerosol components, J. Quant. Spectrosc. Ra., 188, 79-93, https://doi.org/10.1016/j.jqsrt.2016.06.031, 2017.

Park, R. S., Lee, S., Shin, S. K., and Song, C. H.: Contribution of ammonium nitrate to aerosol optical depth and direct radiative forcing by aerosols over East Asia, Atmos. Chem. Phys., 14, 2185-2201, https://doi.org/10.5194/acp-14-2185-2014, 2014.

Randles, C. A., da Silva, A. M., Buchard, V., Colarco, P. R., Darmenov, A., Govindaraju, R., Smirnov, A., Holben, B., Ferrare, R., Hair, J., Shinozuka, Y., and Flynn, C. J.: The MERRA-2 aerosol reanalysis, 1980 onward. Part I: System description and data assimilation evaluation, J. Climate, 30, 6823-6850, https://doi.org/10.1175/JCLI-D-16-0609.1, 2017.

Rodriguez, M. A., Brouwer, J., Samuelsen, G. S., and Dabdub, D.: Air quality impacts of distributed power generation in the South Coast Air Basin of California 2: Model uncertainty and sensitivity analysis, Atmos. Environ., 41, 5618-5635,

941   https://doi.org/10.1016/j.atmosenv.2007.02.049, 2007.

942   Rubin, J. I. and Collins, W. D.: Global simulations of aerosol amount and size using MODIS observations assimilated with an

943   Ensemble Kalman Filter, J. Geophys Res. Atmospheres, 119, 12,780-712,806, https://doi.org/10.1002/2014JD021627, 2014.

944   Rubin, J. I., Reid, J. S., Hansen, J. A., Anderson, J. L., Holben, B. N., Xian, P., Westphal, D. L., and Zhang, J. L.: Assimilation

945   of AERONET and MODIS AOT observations using variational and ensemble data assimilation methods and its impact on

946   aerosol forecasting skill, J. Geophys Res.-Atmospheres, 122, 4967-4992, https://doi.org/10.1002/2016jd026067, 2017.

947   Saide, P. E., Kim, J., Song, C. H., Choi, M., Cheng, Y., and Carmichael, G. R.: Assimilation of next generation geostationary

948   aerosol optical depth retrievals to improve air quality simulations, Geophys. Res. Lett., 41, 9188-9196,

949   https://doi.org/10.1002/2014GL062089, 2014.

950   Sax, T. and Isakov, V.: A case study for assessing uncertainty in local-scale regulatory air quality modeling applications, Atmos.

951   Environ., 37, 3481-3489, https://doi.org/10.1016/S1352-2310(03)00411-4, 2003.

952   Schlesinger, R. B.: The health impact of common inorganic components of fine particulate matter (PM$_{2.5}$) in ambient air: a

953   critical review, Inhal. Toxicol., 19, 811-832, https://doi.org/10.1080/08958370701402382, 2007.

954   Schult, I., Feichter, J., and Cooke, W. F.: Effect of black carbon and sulfate aerosols on the Global Radiation Budget, J. Geophys

955   Res.-Atmospheres, 102, 30107-30117, https://doi.org/10.1029/97jd01863, 1997.

956   Schutgens, N. A. J., Miyoshi, T., Takemura, T., and Nakajima, T.: Applying an ensemble Kalman filter to the assimilation of

957   AERONET observations in a global aerosol transport model, Atmos. Chem. Phys., 10, 2561-2576, https://doi.org/10.5194/acp-

958   10-2561-2010, 2010.

959   Schwartz, C. S., Liu, Z., Lin, H.-C., and Cetola, J. D.: Assimilating aerosol observations with a "hybrid" variational-ensemble

960   data assimilation system, J. Geophys Res.-Atmospheres, 119, 4043-4069, https://doi.org/10.1002/2013jd020937, 2014.

961   Soni, A., Mandariya, A. K., Rajeev, P., Izhar, S., Singh, G. K., Choudhary, V., Qadri, A. M., Gupta, A. D., Singh, A. K., and

962   Gupta, T.: Multiple site ground-based evaluation of carbonaceous aerosol mass concentrations retrieved from CAMS and

963   MERRA-2 over the Indo-Gangetic Plain, Environm. Sci.-Atmos., 1, 577-590, https://doi.org/10.1039/d1ea00067e, 2021.

964   Strebel, L., Bogena, H. R., Vereecken, H., and Hendricks Franssen, H. J.: Coupling the Community Land Model version 5.0

965   to the parallel data assimilation framework PDAF: description and applications, Geosci. Model Dev., 15, 395-411,

966   https://doi.org/10.5194/gmd-15-395-2022, 2022.

967   Su Lee, Y., Choi, E., Park, M., Jo, H., Park, M., Nam, E., Gon Kim, D., Yi, S.-M., and Young Kim, J.: Feature Extraction and

968   Prediction of Fine Particulate Matter (PM$_{2.5}$) Chemical Constituents using Four Machine Learning Models, Expert Syst. Appl.,

969   119696, https://doi.org/10.1016/j.eswa.2023.119696, 2023.

970   Talagrand, O. and Courtier, P.: Variational Assimilation of Meteorological Observations With the Adjoint Vorticity Equation.

971   I: Theory, Q. J. Roy. Meteor. Soc., 113, 1311-1328, https://doi.org/10.1002/qj.49711347812, 1987.

972   Tang, Y., Chai, T., Pan, L., Lee, P., Tong, D., Kim, H. C., and Chen, W.: Using optimal interpolation to assimilate surface

973   measurements and satellite AOD for ozone and PM$_{2.5}$: A case study for July 2011, Journal of the Air and Waste Management

974   Association, 65, 1206-1216, https://doi.org/10.1080/10962247.2015.1062439, 2015.

975   Tippett, M. K., Anderson, J. L., Bishop, C. H., Hamill, T. M., and Whitaker, J. S.: Ensemble Square Root Filters, Mon. Weather

976   Rev., 131, 1485-1490, https://doi.org/10.1175/1520-0493(2003)131<1485:ESRF>2.0.CO;2, 2003.

977   Tödter, J. and Ahrens, B.: A Second-Order Exact Ensemble Square Root Filter for Nonlinear Data Assimilation, Mon. Weather

978   Rev., 143, 1347-1367, https://doi.org/10.1175/MWR-D-14-00108.1, 2015.

979   Tödter, J., Kirchgessner, P., Nerger, L., and Ahrens, B.: Assessment of a Nonlinear Ensemble Transform Filter for High-

980   Dimensional Data Assimilation, Mon. Weather Rev., 144, 409-427, https://doi.org/10.1175/MWR-D-15-0073.1, 2016.

981   Tsikerdekis, A., Schutgens, N. A. J., and Hasekamp, O. P.: Assimilating aerosol optical properties related to size and absorption

982   from POLDER/PARASOL with an ensemble data assimilation system, Atmos. Chem. Phys., 21, 2637-2674,

983   https://doi.org/10.5194/acp-21-2637-2021, 2021.

984   Wang, H., Yang, T., Wang, Z., Li, J., Chai, W., Tang, G., Kong, L., and Chen, X.: An aerosol vertical data assimilation system

985   (NAQPMS-PDAF v1.0): development and application, Geosci. Model Dev., 15, 3555-3585, https://doi.org/10.5194/gmd-15-

986   3555-2022, 2022.

987   Wang, N., H. Guo, Jiang, F., Ling, Z. H., and Wang, T.: Simulation of ozone formation at different elevations in mountainous

area of Hong Kong using WRF-CMAQ model, Sci. Total Environ., 505, 939-951, https://doi.org/10.1016/j.scitotenv.2014.10.070, 2015.

Wang, T., Liu, H., Li, J., Wang, S., Kim, Y., Sun, Y., Yang, W., Du, H., Wang, Z., and Wang, Z.: A two-way coupled regional urban–street network air quality model system for Beijing, China, Geosci. Model Dev., 16, 5585-5599, https://doi.org/10.5194/gmd-16-5585-2023, 2023.

Wang, Z., Itahashi, S., Uno, I., Pan, X., Osada, K., Yamamoto, S., Nishizawa, T., Tamura, K., and Wang, Z.: Modeling the Long-Range Transport of Particulate Matters for January in East Asia using NAQPMS and CMAQ, Aerosol Air Qual. Res., 17, 3065-3078, https://doi.org/10.4209/aaqr.2016.12.0534, 2017.

Wang, Z., Li, J., Wang, Z., Yang, W., Tang, X., Ge, B., Yan, P., Zhu, L., Chen, X., Chen, H., Wand, W., Li, J., Liu, B., Wang, X., Wand, W., Zhao, Y., Lu, N., and Su, D.: Modeling study of regional severe hazes over mid-eastern China in January 2013 and its implications on pollution prevention and control, Sci. China Earth Sci., 57, 3-13, https://doi.org/10.1007/s11430-013-4793-0, 2014.

Wang, Z., Maeda, T., Hayashi, M., Hsiao, L. F., and Liu, K. Y.: A Nested Air Quality Prediction Modeling System for Urban and Regional Scales: Application for High-Ozone Episode in Taiwan, Water Air Soil Poll., 130, 391-396, https://doi.org/10.1023/A:1013833217916, 2001.

Wang, Z., Uno, I., Yumimoto, K., Pan, X., Chen, X., Li, J., Wang, Z., Shimizu, A., and Sugimoto, N.: Dust Heterogeneous Reactions during Long-Range Transport of a Severe Dust Storm in May 2017 over East Asia, Atmosphere, 10, 680, https://doi.org/10.3390/atmos10110680, 2019.

Werner, M., Kryza, M., and Guzikowski, J.: Can Data Assimilation of Surface $PM_{2.5}$ and Satellite AOD Improve WRF-Chem Forecasting? A Case Study for Two Scenarios of Particulate Air Pollution Episodes in Poland, Remote Sens., 11, https://doi.org/10.3390/rs11202364, 2019.

Wilcox, E. M., Thomas, R. M., Praveen, P. S., Pistone, K., Bender, F. A., and Ramanathan, V.: Black carbon solar absorption suppresses turbulence in the atmospheric boundary layer, P. Natl. Acad. Sci. USA, 113, 11794-11799, https://doi.org/10.1073/pnas.1525746113, 2016.

Xia, X., Min, J., Wang, Y., Shen, F., Yang, C., and Sun, Z.: Assimilating Himawari-8 AHI aerosol observations with a rapid-update data assimilation system, Atmos. Environ., 215, https://doi.org/10.1016/j.atmosenv.2019.116866, 2019.

Xia, X., Min, J., Shen, F., Wang, Y., Xu, D., Yang, C., and Zhang, P.: Aerosol data assimilation using data from Fengyun-4A, a next-generation geostationary meteorological satellite, Atmos. Environ., 237, https://doi.org/10.1016/j.atmosenv.2020.117695, 2020.

Xie, X., Hu, J., Qin, M., Guo, S., Hu, M., Wang, H., Lou, S., Li, J., Sun, J., Li, X., Sheng, L., Zhu, J., Chen, G., Yin, J., Fu, W., Huang, C., and Zhang, Y.: Modeling particulate nitrate in China: Current findings and future directions, Environ. Int., 166, 107369, https://doi.org/10.1016/j.envint.2022.107369, 2022.

Yan, Y., Zhou, Y., Kong, S., Lin, J., Wu, J., Zheng, H., Zhang, Z., Song, A., Bai, Y., Ling, Z., Liu, D., and Zhao, T.: Effectiveness of emission control in reducing $PM_{2.5}$ pollution in central China during winter haze episodes under various potential synoptic controls, Atmos. Chem. Phys., 21, 3143-3162, https://doi.org/10.5194/acp-21-3143-2021, 2021.

Yang, T., Li, H., Wang, H., Sun, Y., Chen, X., Wang, F., Xu, L., and Wang, Z.: Vertical aerosol data assimilation technology and application based on satellite and ground lidar: A review and outlook, J. Environ. Sci., 123, 292-305, https://doi.org/10.1016/j.jes.2022.04.012, 2023.

Yang, X., Wu, Q., Zhao, R., Cheng, H., He, H., Ma, Q., Wang, L., and Luo, H.: New method for evaluating winter air quality: $PM_{2.5}$ assessment using Community Multi-Scale Air Quality Modeling (CMAQ) in Xi'an, Atmos. Environ., 211, 18-28, https://doi.org/10.1016/j.atmosenv.2019.04.019, 2019.

Ye, Q., Li, J., Chen, X., Chen, H., Yang, W., Du, H., Pan, X., Tang, X., Wang, W., Zhu, L., Li, J., Wang, Z., and Wang, Z.: High-resolution modeling of the distribution of surface air pollutants and their intercontinental transport by a global tropospheric atmospheric chemistry source–receptor model (GNAQPMS-SM), Geosci. Model Dev., 14, 7573-7604, https://doi.org/10.5194/gmd-14-7573-2021, 2021.

Yu, H. C., Zhang, Y. J., Nerger, L., Lemmen, C., Yu, J. C. S., Chou, T. Y., Chu, C. H., and Terng, C. T.: Development of a flexible data assimilation method in a 3D unstructured-grid ocean model under Earth System Modeling Framework,

1035 EGUsphere [preprint], 2022, 1-29, https://doi.org/10.5194/egusphere-2022-114, 2022.

1036 Zhai, S. X., Jacob, D. J., Wang, X., Shen, L., Li, K., Zhang, Y. Z., Gui, K., Zhao, T. L., and Liao, H.: Fine particulate matter
1037 ($PM_{2.5}$) trends in China, 2013-2018: separating contributions from anthropogenic emissions and meteorology, Atmos. Chem.
1038 Phys., 19, 11031-11041, https://doi.org/10.5194/acp-19-11031-2019, 2019.

1039 Zhang, F., Wang, Z.-w., Cheng, H.-r., Lv, X.-p., Gong, W., Wang, X.-m., and Zhang, G.: Seasonal variations and chemical
1040 characteristics of $PM_{2.5}$ in Wuhan, central China, Sci. Total Environ., 518-519, 97-105,
1041 https://doi.org/10.1016/j.scitotenv.2015.02.054, 2015.

1042 Zhang, J., Reid, J. S., Westphal, D. L., Baker, N. L., and Hyer, E. J.: A system for operational aerosol optical depth data
1043 assimilation over global oceans, J. Geophys Res., 113, https://doi.org/10.1029/2007jd009065, 2008.

1044 Zhang, J., Campbell, J. R., Hyer, E. J., Reid, J. S., Westphal, D. L., and Johnson, R. S.: Evaluating the impact of multisensor
1045 data assimilation on a global aerosol particle transport model, J. Geophys Res.-Atmos., 119, 4674-4689,
1046 https://doi.org/10.1002/2013jd020975, 2014.

1047